Atmos. Chem. Phys. Discuss., 11, 30797–30851, 2011
www.atmos-chem-phys-discuss.net/11/30797/2011/
doi:10.5194/acpd-11-30797-2011

Atmospheric Chemistry and Physics Discussions

Ice formation and development in aged, wintertime cumulus over the UK : observations and modelling

I. Crawford[1], K. N. Bower[1], T. W. Choularton[1], C. Dearden[1], J. Crosier[1,2], C. Westbrook[3], G. Capes[1], H. Coe[1], P. Connolly[1], J. R. Dorsey[1,2], M. W. Gallagher[1], P. Williams[1], J. Trembath[4], Z. Cui[5], and A. Blyth[2,5]

[1]Centre for Atmospheric Science, SEAES, University of Manchester, UK
[2]National Centre for Atmospheric Science, UK
[3]Department of Meteorology, University of Reading, UK
[4]Facility for Airborne Atmospheric Measurements, Cranfield University, UK
[5]School of Earth and Environment, University of Leeds, UK

Received: 12 October 2011 – Accepted: 18 October 2011 – Published: 16 November 2011

Correspondence to: I. Crawford (i.crawford@manchester.ac.uk)

Published by Copernicus Publications on behalf of the European Geosciences Union.

Abstract

In-situ high resolution aircraft measurements of cloud microphysical properties were made in coordination with ground based remote sensing observations of Radar and Lidar as part of the Aerosol Properties, PRocesses And InfluenceS on the Earth's climate (APPRAISE) project. A narrow but extensive line (~100 km long) of shallow convective clouds over the southern UK was studied. Cloud top temperatures were observed to be higher than ~ −8 °C, but the clouds were seen to consist of supercooled droplets and varying concentrations of ice particles. No ice particles were observed to be falling into the cloud tops from above. Current parameterisations of ice nuclei (IN) numbers predict too few particles will be active as ice nuclei to account for ice particle concentrations at the observed near cloud top temperatures (~ −7 °C). The role of biological particles, consistent with concentrations observed near the surface, acting as potential efficient high temperature IN is considered important in this case. It was found that very high concentrations of ice particles (up to 100 L^{-1}) could be produced by powerful secondary ice particle production emphasising the importance of understanding primary ice formation in slightly supercooled clouds.

Aircraft penetrations at −3.5 °C, showed peak ice crystal concentrations of up to 100 L^{-1} which together with the characteristic ice crystal habits observed (generally rimed ice particles and columns) suggested secondary ice production had occurred. To investigate whether the Hallett-Mossop (HM) secondary ice production process could account for these observations, ice splinter production rates were calculated. These calculated rates and observations could only be reconciled provided the constraint that only droplets >24 µm in diameter could lead to splinter production, was relaxed slightly by 2 µm.

Model simulations of the case study were also performed with the WRF (Weather, Research and Forecasting) model and ACPIM (Aerosol Cloud and Precipitation Interactions Model) to investigate the likely origins of the ice phase in these slightly supercooled clouds and to assess the role played by the HM process in this and in controlling precipitation formation under these conditions.

ACPD

11, 30797–30851, 2011

WRF results showed that while HM does act to increase the mass and number concentration of ice particles produced in the model simulations, in the absence of HM, the ice number concentration arising from primary ice nucleation alone (several L^{-1}) was apparently sufficient to sustain precipitation although the distribution of the precipitation was changed. Thus in the WRF model the HM process was shown to be non-critical for the formation of precipitation in this particular case. However, this result is seen to be subject to an important caveat concerning the simulation of the cloud macrostructure. The model was unable to capture a sharp temperature inversion seen in the radiosonde profiles at 2 km, and consequently the cloud top temperature in the model was able to reach lower values than observed in-situ or obtained from satellite data. ACPIM simulations confirmed the HM process to be a very powerful mechanism for producing the observed high ice concentrations, provided that primary nucleation occured to initiate the ice formation, and large droplets were present which then fell collecting the primary ice particles to form instant rimer particles. However, the time to generate the observed peak ice concentrations was found to be dependant on the number of primary IN present (decreasing with increasing IN number). This became realistic (around 20 min) only when the temperature input to the existing IN parameterisation was 6 °C lower than observed at cloud top, highlighting the requirement to improve basic knowledge of the number and type of IN active at these high temperatures. In simulations where cloud droplet numbers were realistic the precipitation rate was found to be unaffected by HM, with warm rain processes dominating precipitation development in this instance.

1 Introduction

Clouds and their interaction with radiation play an important part in the earth's climate. The formation of cloud particles and their interactions with aerosol are highly uncertain (Forster et al., 2007), with the formation and evolution of mixed phase and ice clouds being particularly poorly understood (Penner et al., 2001).

ACPD
11, 30797–30851, 2011

Consequently there has been extensive work over the past few years to explain the observed numbers of ice crystals within clouds (Phillips et al., 2008; Connolly et al., 2009; DeMott et al., 2010). These studies have been motivated partially by observations of ice in clouds from field campaigns and also to develop parameterisations within atmospheric models. One field study in particular, which was based in the Florida region, noted the glaciation of an altocumulus cloud at −5 °C and correlated this to dust from the Sahara which had advected into the region by long range transport in easterly winds over the Atlantic (Sassen et al., 2003). They postulated that the dust may have been acting as an effective ice nucleus at these high temperatures. Dust particles are generally considered to be an efficient IN however, more recent field and laboratory investigations have suggested desert dusts are not particularly effective IN at such high temperatures. For instance, in a study involving lidar depolarisation measurements of short lived alto-cumulus clouds over Morocco, Ansmann et al. (2008) noted that ice was hardly ever observed in these clouds when the temperature was higher than −20 °C, and even then almost never when liquid water was not also observed to be present. Ansmann et al.'s study highlights that, in the atmosphere, ice nucleation at relatively high temperatures mainly acts when liquid water is present first, rather than by the heterogeneous deposition mechanism, and that nucleation on desert dust occurs once the temperature is lower than roughly −20 °C. A four year remote sensing study by Westbrook and Illingworth (2011) found that 95 % of the ice particles formed in layer clouds over the southern UK at $T > -20$ °C were formed in supercooled liquid clouds. The likely candidates that may describe such ice nucleation are: (i) condensation-freezing; (ii) immersion-freezing or contact nucleation. Ansmann et al.'s study was subsequently backed up by laboratory studies on a range of desert dust particles e.g. Connolly et al. (2009), who showed that three different dusts nucleated ice in appreciable amounts at $T \sim -20$ °C and that there was no significant nucleation if liquid water did not form on the dust first. It is therefore unclear what the effective atmospheric ice nuclei are at temperatures higher than ∼ −10 °C. However, these laboratory studies were conducted with dust samples collected at source and which therefore had likely not undergone

ACPD
11, 30797–30851, 2011

any physico-chemical modification as a result of atmospheric transport, which could lead to alteration of its ice nucleation properties.

The ability of biological particles to act as more effective IN than dust at warm temperatures has been also been considered. Such particles include bacteria, pollen and fungal spores. Calculations of the relative efficiency of various IN including biological particles will be presented and discussed in association with biological particle concentration measurements at the surface that were also carried out as part of the APPRAISE field project.

Existing ice nucleation parameterisations that have been used to quantify numbers of atmospheric ice nuclei at such high temperatures typically predict fairly low numbers of ice nuclei (IN). For instance, the widely used Meyers et al. (1992) scheme, for condensation/deposition nucleation, predicts that at water saturation there are $1\,L^{-1}$ of ice crystals at $-10\,^{\circ}C$ and $9\,L^{-1}$ at $-20\,^{\circ}C$. More recently, an ice nucleation parameterisation was developed by DeMott et al. (2010) that depends on the number of aerosol with diameters larger than 0.5 µm diameter and the temperature. If we consider a typical continental distribution of aerosols, described by lognormal distribution parameters of $\sigma_g = 2.03$, $D_N = 0.069\,\mu m$, $N_L = 1.3 \times 10^4\,cm^{-3}$ (Whitby, 1978), then the number of aerosols larger than 0.5 µm is $33\,cm^{-1}$ and the corresponding number of ice crystals predicted by the new scheme is $0.3\,L^{-1}$ at $-10\,^{\circ}C$ and $9\,L^{-1}$ at $20\,^{\circ}C$, which is similar to that predicted by the earlier Meyers et al. scheme. Even though the schemes predict relatively few primary IN, there is strong evidence to show that ice crystal concentrations in this temperature regime frequently exceed this by in some cases 4 orders of magnitude (c.f. Table in Mossop, 1978). A commonly invoked explanation is secondary ice production by the Hallett-Mossop process (HM) (DeMott et al., 2003; Mossop et al., 1972; Blyth and Latham, 1993; Bower et al., 1996; Hogan et al., 2002; Huang et al., 2009; Crosier et al., 2011). Hallett and Mossop (1974) showed that secondary ice production occurs during riming at slightly supercooled temperatures ($-3\,^{\circ}C$ to $-8\,^{\circ}C$) by rime splintering. Further investigations proposed that the supercooled droplet population must contain droplets smaller than 13 µm in diameter and larger

ACPD
11, 30797–30851, 2011

than 24 µm for the process to occur (Mossop (1978); Saunders and Hosseini (2001)).

In this study, multi-level penetrations of convective cumulus clouds were made by the BAe146 Facility for Airborne Atmospheric Measurement (FAAM) aircraft in conjunction with simultaneous remote sensing measurements from the UK Met Office operational radar network and the Chilbolton Facility for Atmospheric and Radio Research (CFARR, 1.44 W, 51.14 N). Based at CFARR and used in this study are: (i) a steerable 3 GHz S-band dual-polarisation radar (the Chilbolton Advanced Meteorological Radar, hereafter called CAMRa, Goddard et al. (1994))); (ii) a 35 GHz vertically pointing cloud radar, and (iii) a vertically pointing lidar ceilometer ($\lambda = 905$ nm). The latter two instruments are described in detail by Illingworth et al. (2007). At 3 GHz, CAMRa is mainly sensitive to larger precipitation sized hydrometeors. However its Doppler capability enables it to provide the radial velocity of these particles towards/away from CFARR whilst undertaking horizontal or vertical scanning patterns. The higher frequency of the vertical pointing radar makes it sensitive to smaller cloud droplets and ice particles in addition to the larger particles observed by CAMRa. The lidar is particularly sensitive to liquid water cloud but as a result suffers attenuation in cloud or rain, seeing only the lowest levels of thick liquid clouds or the precipitation falling out from the base of cloud systems.

1.1 Sampling strategy

On the 22 January 2009, the microphysical properties of a narrow line of shallow convective clouds were investigated as this line advected towards, and then over, CFARR. The FAAM BAe146 aircraft (flight reference B425) flew a series of runs at increasing altitude to sample the convective cloud at many levels from cloud base to cloud top. These runs are summarised in Table 1. Aircraft operations were restricted by air traffic control to an area to the west of CFARR (see Fig. 1) where the aircraft flew at multiple levels along a radial of 253° from CFARR, from overhead the facility to a range of 100 km out to the west. CAMRa performed a series of Range Height Indicator (RHI) scans along this radial while the 35 GHz radar and lidar ceilometer gathered

ACPD
11, 30797–30851, 2011

data vertically overhead. Real-time communication of radar and lidar data to the aircraft allowed coordination of the in situ measurements with key features identified by the remote sensing instrumentation.

The FAAM BAe146 aircraft was fitted with a wide array of cloud spectrometers, meteorological sensors and aerosol and trace gas instruments. 1 Hz measurements of GPS position, temperature (de-iced and non de-iced Rosemount sensors), ambient pressure and dew point temperature (General Eastern and Buck CR2 chilled mirror hygrometers) were made along with horizontal and vertical wind speed (also available at 32 Hz resolution) using a 5-hole pressure port turbulence probe. Additionally, the aerosol particle size distribution was measured with a pylon mounted PMS (Particle Measuring Systems) PCASP-100 (size range 0.1–3.0 µm). Size-segregated and chemically speciated mass composition measurements of sub-micron aerosol (30 nm-1 µm) were made with a Compact Time-of-Flight Aerosol Mass Spectrometer (C-ToF-AMS, Aerodyne Research Inc.) sampling through a Rosemount inlet. Also sampling from the Rosemount inlet was a DMT (Droplet Measurement Technologies) dual column cloud condensation nuclei counter (DMT CCN-200) operated at set supersaturations of 0.12 % and 0.08 % in the separate columns respectively. These data were used to constrain aerosol inputs for a modelling sensitivity study described later.

Cloud droplet number size distribution measurements ($2< d_p <50$ µm) were made using a Cloud Droplet Probe (CDP-100, DMT), a Cloud and Aerosol Spectrometer (CAS, DMT modified version, size range $0.5< d_p <50$ µm) and a Forward Scattering Spectrometer Probe (FSSP SPP-100, DMT, size range $2< d_p <47$ µm). Because of the possibility of shattering artefacts due to ice particle break up on the inlet in mixed-phase conditions, data from the CAS and FSSP are not considered here, however, the open path CDP data were used (see McFarquhar et al. (2007)). The limitations of this instrument are described in greater detail by Lance et al. (2010). Ice and large cloud droplets together with drizzle droplets were measured using a CCD imaging probe (SPEC CPI) and several 2-D optical array probes (OAPs). These included a SPEC Inc 2DS-128-H (herein referred to as 2DS, described in Lawson et al., 2006) and a DMT CIP-100

ACPD
11, 30797–30851, 2011

(Cloud Imaging Probe-100) optical array probe. The 2DS has 128 1-bit elements and a resolution of 10 µm covering a particle size range of approximately 10-1280 µm. Data from this instrument were used for the bulk of the ice and drizzle particle analyses in this paper. The DMT CIP-100 has 64 elements of 100 µm resolution each, and thus images particles in the size range 100–6400 µm. Data from this instrument were used to determine the presence of large precipitation particles. Further details of the instruments, the data processing techniques and corrections applied to the OAP probes to derive ice water contents are provided in Crosier et al. (2011).

2 Shallow convection on the Chilbolton radial

2.1 Meteorological conditions

On the 22 January 2009 there was a region of lower pressure to the north-west of the UK between Iceland and Ireland, with higher pressure to the east over Europe. Earlier, a series of warm fronts crossed the UK; one the previous day and a second in the early morning which was closely followed by a cold front. By midday, prior to take off, troughs were observed over London and the west coast of Ireland. The Met Office operational radar network showed two north-south orientated bands of precipitation moving to the east which had precipitated over the UK earlier in the morning. At the time of take-off (13:15 UTC) a thin band of cloud orientated east-west passed over the UK with rainfall rates of up to approximately 3 mm h^{-1}. The aircraft profile of temperature and dew point temperature showed there to be a moist layer between 1.6 and 2.2 km with a dry layer between 2.2 and 2.5 km. This was in good agreement with measurements from the midday radiosonde releases from Cambourne and nearby Larkhill (see Fig. 1).

2.2 Cloud properties

Figure 2 shows a time series of the 35 GHz vertically pointing radar reflectivity and lidar backscatter coefficient at CFARR. The line of cloud measured with the FAAM aircraft

ACPD
11, 30797–30851, 2011

started to pass over the radar at around 14:00 UTC. Both the radar and lidar observed drizzle below 1 km from just before 14:30 UTC until around 15:00 UTC. The reflectivity from this liquid precipitation peaked at around 30 dBZ, corresponding to a rain rate of several mm per hour.

The typical cloud properties observed at each level of the series of constant altitude runs (Table 1) are summarized in Fig. 3. The first run R1 (Altitude = 1.30 km, $T = -1\,^{\circ}\mathrm{C}$) was performed inbound to CFARR in cloud while the reciprocal run R2 was performed outbound from CFARR below cloud (Altitude = 0.75 km, $T = +2.7\,^{\circ}\mathrm{C}$). R2 intersected a band of precipitation which contained low concentrations ($0.002\,\mathrm{L}^{-1}$) of spheroidal particles with observed volume mode diameters ranging from 200 to 600 µm and rain rates of up to $4\,\mathrm{mm\,h}^{-1}$ at a distance of 28 to 50 km from the Chilbolton observatory. For the majority of the run the CDP droplet number concentration was approximately zero. These observations (e.g. of cloud base height and the presence of drizzle below cloud) are in agreement with the observations from the vertical pointing radar shown in Fig. 2.

Figures 4 and 5 show the altitude of the aircraft overlaid on RHI scans from CAMRa along the 253° radial for the first in-cloud runs, R1 and R3 (inbound to Chilbolton, Altitude = 1.26 km, $T = -3.5\,^{\circ}\mathrm{C}$), respectively. Here the RHI scan closet in time to each cloud penetration is chosen for comparison. As for runs R1 and R3, the RHI scans of runs R2 and R4 (not shown) found the sampled clouds to be comprised of many cells with reflectivities ranging from approximately 0 to +30 dBz. A bright band in the reflectivity, which signifies the melting layer, was seen in the CAMRa RHI scans from around 13:58 onwards, at an altitude slightly less than 1 km (see Fig. 5 for R3). There was a corresponding enhancement in differential reflectivity at the same level (not shown) However, the bright band, corresponding to the melting of ice particles as they pass through the 0 °C level, appears to be quite weak or absent through a lot of the cloud sampled. This suggests that the radar signal is largely dominated by graupel or heavily rimed crystals in the parts producing the precipitation. This is in contrast to a situation where a much stronger bright band effect would be produced by melting snow flakes

ACPD
11, 30797–30851, 2011

passing through this level. Subsequent RHI scans do show some enhancement (over that of R3) in the bright band and differential reflectivity at around this level.

Figures 4 and 5 also show key microphysical measurements made by the aircraft during runs R1 and R3 (the two earliest in cloud runs both inbound to CFARR). During R1, droplet number concentrations of around 150 cm^{-3} were observed (Fig. 4). Concentrations of drizzle droplets of a few per litre were also observed although these contributed much less to the condensed water content than the smaller droplets. This run encountered these cells in the line of clouds at an early stage of development. The layer of weak reflectivity in the nearest 30 km to CFARR (Fig. 4) is actually an echo from the base of the inversion, caused by the turbulent mixing of the dry air in the free troposphere and the moister air in the boundary layer, Morcrette et al. (2007). The potential for turbulent loss of aerosol particles across this inversion is discussed later.

In the second in-cloud run R3 (Fig. 5), the line of clouds was encountered 45 min later (than during R1), and a greater number of cells were intercepted, and many of these cells were more "developed". The radar reflectivities were higher, and the clouds contained both liquid and ice in varying amounts. Over the first 10 km of the in-cloud section of the run, the turbulence intensity was relatively lower than the run average (mean vertical velocity, $w = 0.15\,ms^{-1}$, $\sigma = 0.55\,ms^{-1}$; in-cloud average, $w = 0.55\,ms^{-1}$, $\sigma = 0.71\,ms^{-1}$). Continuous cloud was observed from 42.5 km west of CFARR but the degree of glaciation often varied considerably between adjacent regions and was sometimes seen to undergo rapid transitions as the aircraft passed through cells (and parts of cells) in different stages of evolution and after potentially mixing with air from previous cells (in varying amounts). At the start of the cloud penetration, 42.5 km out from CFARR, the cloud was mixed phase in nature, containing a few tens per cm^3 of droplets and approximately 20 L^{-1} of rimed ice particles. 38.2 km from CFARR the ice crystal number doubled and no droplets were detected by the CDP or imaged by the 2DS. Images of crystals in this region showed them to be comprised of rimed columns and aggregates. Directly following this, a region was encountered comprised of a short burst of high concentrations of supercooled droplets (up to 150 cm^{-3}) coexisting with

ACPD
11, 30797–30851, 2011

only a few per litre of ice particles, all within a distance of only 400 m. CAMRa gave a weak echo at this position. An extensive mixed phase region containing rimed ice and columns of relatively high ice crystal number concentration (20 to 100 L^{-1}) then persisted for 8.3 km before another supercooled region was encountered. This largely supercooled liquid region spanned approximately 11.2 km but unlike the previous regions, prolonged updrafts were also encountered with typical vertical velocities of between 1–2 m s^{-1}, with associated peak liquid water contents of up to 1 g m^{-3} in the strongest updrafts. Rimed ice particles were also present in this region in concentrations of 1–10 L^{-1}, and the radar echo here was around 15–20 dBZ. A further mixed phase region, quiescent in nature, consisting of rimed ice and small columns followed. Mixed phase conditions were then encountered at a distance of 18.3 km from CFARR and persisted for 5.3 km with peak ice crystal number concentrations of up to 80 L^{-1} and ice water contents of approximately 0.2 g m^{-3}. Beyond this (i.e. closer to CFARR), the cloud was mainly comprised of supercooled liquid with some drizzle drops present. 2DS imagery showed no ice present.

On the next in-cloud run (R4, outbound from CFARR, altitude = 1.93 km, $T = -6\,^{\circ}C$) at a distance of 13 to 20 km from CFARR, graupel and pristine column crystals were observed, the latter in concentrations of 100–200 L^{-1},with corresponding ice water contents of 0.5–1 g m^{-3}. Low concentrations of supercooled droplets were also present (up to 25 cm^{-3}). Heavy riming (and freezing of water within the ports) of the turbulence probe made subsequent wind measurements unreliable for the remainder of this run. 30 km from CFARR the droplet concentration increased to 50 cm^{-3} and continued to increase to around 100 cm^{-3} over the next 6 km while the ice crystal concentration reduced to zero.

ACPD
11, 30797–30851, 2011

A run was also performed at cloud top (R5: $T = -7.5\,^{\circ}\mathrm{C}$) at an altitude of 2.24 km. A mixed phase feature 10.1 to 22.1 km from CFARR displayed typical ice concentrations of less than $20\,\mathrm{L}^{-1}$ with ice water contents less than $0.1\,\mathrm{g\,m}^{-3}$. A few small regions showed enhancements of ice concentrations exceeding $100\,\mathrm{L}^{-1}$ and ice water contents of $0.5\,\mathrm{g\,m}^{-3}$. The ice particles in these regions were of similar habit to those of previous runs. Within this run supercooled droplets were present at low concentrations (10–$30\,\mathrm{cm}^{-3}$) and liquid water contents were typically in the range of 0.05–$0.2\,\mathrm{g\,m}^{-3}$.

Runs R6 and R7 were subsequently performed above cloud to assess potential seeding from above at altitudes of 2.54 km and 2.24 km respectively. However none of the cloud spectrometers detected any particles within their capabilities, thus making the possibility of ice seeding initiating glaciation in these clouds from an above cloud source unlikely. This is also supported by the radar scans and vertical profiles.

2.3 In-situ aerosol properties

Aerosol measurements showed the operational area to be representative of clean air mass types. Below cloud base the mean PCASP aerosol number concentration was around $120\,\mathrm{cm}^{-3}$ (run R2, Altitude = 0.75 km). A run above cloud top (R6, Altitude = 2.54 km) found the aerosol number concentration had diminished to $\sim 10\,\mathrm{cm}^{-3}$. The sub-micron aerosol mass composition on average below cloud, as measured by the C-ToF-AMS, was: $0.28\,\mu\mathrm{g\,m}^{-3}$ of organic aerosol; $0.11\,\mu\mathrm{g\,m}^{-3}$ of sulphate; and NH_4^+ and NO_3^- each contributed approximately $0.05\,\mu\mathrm{g\,m}^{-3}$ to the total. The relative aerosol composition breakdown observed during run R2 was very similar to that measured at the CFARR ground site (again with a C-ToF-AMS) during the first half of the flight. In each case, organic aerosol represented around 50 % of the total mass, sulphate contributed 25 %, nitrate 10 %, with varying contributions from other species. The organic mass spectra showed the same ordering of *m/z* peaks in each case and indicated a mixture of combustion sources (solid fuel burning and vehicle emissions) together with a more atmospherically aged component. Accompanying aerosol size distribution measurements were also made on the ground at CFAAR with a Scanning

ACPD
11, 30797–30851, 2011

Mobility Particle Sizer (SMPS, TSI model 3080L), a GRIMM optical particle counter (model 1.108) and a dual-Wavelength Integrating Bio-Aerosol Spectrometer, WIBS-3 (Kaye et al., 2005; Gabey et al., 2010). The WIBS detected material consistent with primary fluorescent biological aerosol particles (PBAP), with modal diameters between ~1.5 µm to 2.5 µm. The potential for these particles to act as ice nuclei at slightly supercooled temperatures is discussed later. However, no PBAB measurements were made on the aircraft so no direct comparison is possible. Comparison of the average aerosol size distribution measured throughout the duration of the flight at the ground site with those from the below cloud run on the aircraft, show similar concentrations across their overlapping size ranges for the SMPS and PCASP (Fig. 6), suggesting that the air at the ground was coupled to and representative of the air just below the base of the cloud. This was confirmed by the Doppler cloud radar measurements which were limited to heights above 500m. Doppler velocity variances were used to determine the turbulence profile and estimate eddy dissipation rates using the technique described by Bouniol et al. (2003). Dissipation rates in excess of 10^{-4} m^2 s^{-3} were observed at all levels through the cloud showing that mixing was occurring from cloud top down to near surface, hence aerosol properties should be similar.

2.3.1 Coupling of observed surface and Airborne Aerosol Measurements

To test this further the Aerosol-Cloud and Precipitation Interactions Model (ACPIM) in a parcel model configuration was used. ACPIM is a section aerosol and microphysics model, which includes detailed treatments of the liquid and ice phases (Connolly et al., 2009).

ACPIM was initialised with the aerosol size distribution and chemical composition measured at the ground, and used to predict the number of CCN in the air just below cloud base for different updraft speeds, based on the aircraft in situ measured turbulence velocities (described below). AMS measurements showed the aerosols measured both at the ground and on the aircraft (during out of cloud runs) were dominated by organic material. A Positive Matrix Factorisation (PMF, Ulbrich et al., 2009) analysis

ACPD
11, 30797–30851, 2011

of the aerosol suggested that the composition breakdown of the organic components was approximately: 50 % of biomass origin; 33 % hydrocarbon like organic aerosol (HOA) and 17 % more oxygenated organic aerosol (OOA). Hygroscopic Tandem Differential Mobility Analyser (HTDMA) data suggested that there were two modes of different hygroscopicity, suggesting that the aerosol were externally mixed. It is likely that the biomass would form one internal mode and the HOA and OOA would be internally mixed with the ammonium sulphate and nitrate, which were present as 25 and 10 % of the total (organic and inorganic) aerosol mass. In the absence of further information, Fulvic acid was used as the representative of both the biomass burning aerosol and the mixture of HOA and OOA. To input the aerosol size distribution, 3 log-normal modes were fitted to the observed composite size distribution measured at the ground. Figure 6c shows the observed data, plus the log normal fits. The lognormal fit parameters are provided in the legend.

Sensitivity studies were undertaken to try to ascertain the importance of aerosol composition to the CCN activity. Four cases were examined: (i) for a composition of pure ammonium sulphate; (ii) for a composition of pure fulvic acid; (iii) for an internal mixture comprised of ammonium sulphate (25 % by mass); ammonium nitrate (10 % by mass) and Fulvic acid (65 % by mass); (iv) for a case comprised of the same mass ratio of components as in (iii) but separated out into an external mixture of two aerosol modes: one composed of pure Fulvic acid and containing half of the total Fulvic acid mass (i.e. 32.5 % of the total aerosol mass); and another consisting of an internal mixture containing the remaining 67.5 % of the total aerosol mass, comprised of the remaining Fulvic acid (32.5 %) and the two inorganic components (25 % and 10 % of the total mass, for sulphate and nitrate respectively), i.e. an internal mixture of Fulvic acid, ammonium sulphate and ammonium nitrate, with the mass percentage ratios of 48.15 : 37.04 : 14.81 respectively. For the two external modes there was no information on how they were size segregated so in the absence of this information the relative fractions of both external mixtures were kept constant across the whole size distribution.

ACPD
11, 30797–30851, 2011

The model was run for 9 different constant updraft speeds (0.01, 0.03, 0.05, 0.1, 0.2, 0.5, 1.0, 2.0 and 2.5 m s^{-1}), starting at 950 mbar and +1 °C at an RH of 95 %, and in each case, ascents of 400 m were undertaken. No ice phase processes were switched on in these simulations as they were primarily to test the description of the aerosol activation process within the model, while using as much ground based data as was possible. From the model output the maximum super saturation attained against the number of particles that were activated above cloud base is plotted for each of the four composition cases (Fig. 7). Data from a dual column CCN instrument during the below cloud run R2 (at 750 m altitude), were used for comparison. At the two supersaturations used (0.08 and 0.12 %), the average CCN concentrations were 30 and 54 cm^{-3} respectively. These two data points are shown plotted together with the model simulations in Fig. 7. This shows that the best agreement between model and data was found when assuming an external mixture. For this case there is no significant difference between assuming aerosol are all internally mixed or that they exist as an external mixture, however, the presence of the organic component was important in reducing the overall CCN activity.

Probability density analysis of the aircraft measured 32 Hz vertical wind speeds in-cloud through run R1 yielded a modal value of 0.6 ms^{-1}. This relates to an activated droplet number concentration of approximately 350 cm^{-3} for the ACPIM parcel model, significantly higher than the observations of droplet number concentration which peak at ~150 cm^{-3} (Fig. 3). In the same regions the liquid water content was found to be close to adiabatic with 1 g m^{-3} at −5 °C (with cloud base at 0 °C). The radiosonde temperature sounding from nearby Larkhill (Fig. 8) showed a slight inversion (~2 to 3 degrees in potential temperature) at ~1 km, just below cloud base, for this case study; note that this inversion is not present in the WRF simulation (described below) as WRF was run from a global meteorological analysis, which tends to smooth out such gradients. However, the effect that the slight inversion may have on transport of material between the boundary layer and free-troposphere is likely to be responsible for the discrepancy between predicted and measured cloud drop number. The results of

ACPD
11, 30797–30851, 2011

a detailed modelling study simulating the passage of a thermal bubble (containing a tracer) propagating up through the inversion suggested only 1/6 of the aerosol population would be transported across the inversion and into the cloud base layer. As indicated previously, CAMRa observed a layer of weak reflectivity (in the cloud free region) in the nearest 30 km to CFARR at the time of R1 (Fig. 4). This was identified as being an echo from the base of the inversion, caused by the turbulent mixing of the dry air from the free troposphere with the moister air in the boundary layer (e.g. Morcrette et al., 2007) and so is consistent with the above calculation of aerosol loss across this layer.

No filter samples were taken on the aircraft during this case study, however nucleopore filters were exposed at the ground site, and these were analysed using an automated scanning electron microscope (SEM) and X-Ray Diffraction (XRD). Most of the detected particles had compositions and morphologies indicative of sea salt. After sea salt, the most frequently identified elements in these particles were Fe, Si and Al, which are found in abundance in mineral dusts. Those particles that were predominantly mineral dust in composition had equivalent area diameters of up to 5 µm. Sea salt aerosols were found with diameters up to 10 µm. The size distributions for all particles, and for those identified as mineral dust (from the SEM-XRD analysis) are shown in Fig. 6b, where the lognormal fits to the size distribution data are also given. Note that mineral dust was generally present for sizes larger than 0.6 µm (Fig. 6) and up to 5 µm. Integrating the size distributions between 0.6 and 5 µm, yields a total number concentration of 10 cm^{-3}, which is sufficiently small that it is unlikely to affect the CCN number calculations appreciably.

In summary, the aerosols measured at the ground are strongly linked to the aerosols at 750 m, but it appears that the slight inversion just below cloud base results in reduced aerosol concentrations interacting with the cloud via entrainment. The limited modelling undertaken here suggests the aerosol concentration transported into cloud on this occasion was ~1/6th of the boundary layer concentration below the inversion.

ACPD
11, 30797–30851, 2011

2.4 Sensitivity Studies of the HM Mechanism using WRF

Numerical modelling studies can provide useful insight in terms of identifying the dominant microphysical processes that occur in clouds. In this instance, results from a numerical model are used to complement the in-situ observations, specifically to address the issue of how important the Hallett-Mossop process is in terms of the evolution of the boundary layer cloud and subsequent precipitation. Simulations of case study B425 were performed using the WRF (Weather Research and Forecasting) model (Version 3.1.1). The outermost domain had a horizontal resolution of 9 km, with a time-step of 18 s. The second domain was configured with a 3:1 ratio, giving a 3 km resolution and this used a 6 s time-step (see Fig. 1). Finally the 3rd and innermost domain focused on the observation region and was configured with a 1 km resolution and 3 s time-step. The model was initialized at 00:00 UTC, 22 January 2009 with NCEP analysis data at 1 degree horizontal resolution. Boundary conditions for the outer domain were also constrained by the NCEP analyses and were updated every 6 h. The analysis data were interpolated onto 80 vertical levels, with a model top at 20 km. The model was configured for one-way nesting such that the inner domains did not feed back onto the parent domains. For the microphysical processes, the Morrison bulk scheme (Morrison et al., 2005) was implemented. This contains dual-moment representations of cloud liquid water, rain, cloud ice, snow and graupel. A gamma distribution is used to describe the cloud droplet size distribution, with a diagnostic relation for the distribution shape parameter; for all other hydrometeors the Marshall and Palmer (1948) distribution is used, which implicitly assumes a shape parameter equal to zero.

An initial 24 h simulation was performed with WRF, and the cloud reflectivity was calculated at the grid point closest to Chilbolton (51.15° N, 1.45° W) within the innermost domain, to allow for comparison with the reflectivity time series as measured using the vertically pointing radar. The model reflectivity was diagnosed from the 6th moment of the size distribution for precipitation-sized particles (i.e. rain, snow and graupel), and calculated from the model output at 30 min intervals where an acceptable simulation

ACPD
11, 30797–30851, 2011

was provided in terms of the cloud structure and the general synoptic conditions. The large-scale frontal systems present overnight and throughout the morning were well simulated by WRF. The most interesting aspect of the simulation appears to be the presence of a strong reflectivity signature at around 14:30 UTC, which is consistent with the onset of convection over Chilbolton as seen by the radar. In-situ observations of the cloud indicate that the peak concentration of droplets was ~150 cm^{-3}. A simulation was performed using the Morrison microphysics scheme, and a single-moment treatment of liquid droplets, with a fixed droplet number concentration of 150 cm^{-3} (it should be noted that the sensitivity of the simulated cloud to the treatment of the liquid phase e.g. using either a double or single moment scheme, was found to be small, and does not alter the fundamental conclusions discussed later). From 12:00 UTC onwards the temporal resolution of the model output was also increased from 30 min to 5 min in order to facilitate a more rigorous comparison with the radar observations. A simulation of the vertical pointing radar reflectivity was than compared with the observed data. Again, the timing of convection was well captured by the model, although the simulated cloud top was slightly higher. This can be explained through analysis of model temperature profiles vs. radiosonde data for selected locations at 12:00 UTC This shows that the model was not able to capture the sharp inversion at around 2 km which was clearly present in the radiosonde profiles (Fig. 8). This failure is likely due to insufficient vertical resolution in the model. Further analysis of the model fields revealed that the convective cloud system was fully developed over the Devon and Cornwall peninsula by 12:00 UTC and this was advected eastwards where it reached the Chilbolton region at around 14:30 UTC. Meridional cross-sections through the simulated cloud taken at a latitude of 51°N at 12:00 UTC (Fig. 9) reveal the mixed-phase nature of the cloud and that it is also producing precipitation at this time. This appears to originate from the ice-phase and then melts to form rain below cloud base (~1 km).

In the Morrison scheme, the HM process can activate in the temperature range between −3 °C and −8 °C, but depends on the mass of supercooled liquid (both cloud liquid water and rain) available for riming. Rime splintering acts to increase both the

ACPD
11, 30797–30851, 2011

mass and number of the cloud ice category, and can act on both snow and graupel depending on which categories are present. Growth of snow through riming of cloud water converts it to graupel, independent of the HM process. An additional simulation was performed where the HM process was switched off from the start of the run (00:00 UTC, 22 January 2009) and the results were compared directly to the simulation where HM was included. Figure 10 (top and middle panels) shows that, by 12:00 UTC, a considerable reduction is noticeable in both snow mass and number due to the effect of switching off the HM process. In particular, the snow number concentration reduces from peak values of $\sim$15 000 kg^{-1} to less than 1000 kg^{-1}. Figure 10 (bottom panels) shows the effect HM has on the graupel number concentration. The graupel number concentrations, even in the absence of HM, still reach up to 5000 kg^{-1} (with concentrations of $\sim$ several per litre) at 12:00 UTC. The impact on precipitation at 14:30 UTC is shown in Fig. 11. Switching off HM leads to a reduction in the spatial extent of the precipitation produced; however, there is no significant reduction in the maximum intensity and therefore the HM process does not appear to be critical to the production of precipitation in this particular simulation. This suggests that the graupel number concentrations in the absence of HM are enough to sustain the precipitation, where graupel is formed through the growth of snow by riming. Additional simulations (not shown) revealed that disabling the graupel category, such that the solid phase is represented by simply cloud ice and snow, results in an increase in snow mass due to conservation of total water. However there is a shift in the size distribution towards larger, fewer snowflakes (1 L^{-1}) due to aggregation (the lack of a self-collection term for graupel explains the higher number concentrations when graupel is included). The impact of this change in size and habit of ice crystals on surface precipitation was small, suggesting that the simulated shallow convective cloud is largely insensitive to the categorisation of ice. A further test with all ice processes switched off resulted in considerably reduced precipitation, and most notably a distinct lack of precipitation over the Chilbolton area by 14:30 UTC. Thus it can be concluded that for this particular case, the model is apparently able to sustain precipitation solely via the parameterized

ACPD
11, 30797–30851, 2011

mechanisms of primary ice nucleation, and that this result does not depend strongly on the subsequent ice growth mechanisms. This naturally poses a new question – what is the source of the predicted primary ice in the model?

Primary ice nucleation in the version of the Morrison scheme used in this study includes two mechanisms. The first of these is based on the parameterization of Cooper (1986), and is permitted to occur at all temperatures colder than −8 °C or, if the supersaturation with respect to ice exceeds 8 %. The concentration of ice crystals predicted by this parameterization is limited to a maximum value of 500 L^{-1} to prevent unrealistically high concentrations at colder temperatures. If the predicted concentration of new ice crystals from the Cooper scheme is less than the concentration of ice particles already present, no additional ice particles are allowed to form via this scheme. Based on the coldest cloud top temperature in the model simulation (−14°C), the ice crystal concentration predicted by the Cooper (1986) parameterization is 0.35 L^{-1}. This is approximately 6 times larger than the parameterised concentration predicted for the observed cloud top temperature (∼ −8°C). The second mechanism by which primary ice can form in the scheme, is based on the freezing of supercooled liquid, with separate treatments for cloud liquid droplets and rain. The freezing parameterizations are allowed to contribute if the temperature is below −4°C and if there is liquid water and/or rain present. The mass and number of raindrops that freeze is then determined from the parameterization of immersion freezing (from Bigg, 1953). In the case of cloud droplets, freezing can also occur due to contact freezing (where the number of contact IN is obtained from Meyers et al., 1992), in addition to immersion freezing. Due to the stochastic nature of the both the contact and immersion freezing parameterizations, drop freezing in the model operates independently of the existing total ice crystal concentration, and is limited only by the number concentration of liquid drops available. Thus new ice crystals can continue to be produced by drop freezing so long as there is supercooled liquid present and the temperature is cold enough.

Repeated simulations were performed with the model to isolate the contribution from each primary ice nucleation scheme to the total ice crystal concentration and the

ACPD
11, 30797–30851, 2011

subsequent impact on precipitation. This was done by switching off each nucleation scheme in turn to isolate the effect of the other (NB – freezing of droplets is treated as a single mechanism from the combined effect of both contact freezing and immersion freezing schemes together). The HM process was left switched off for these simulations to focus purely on primary ice. Additional diagnostics were also output from the model every 15 min, to quantify the instantaneous ice number concentration tendency from both the Cooper scheme and drop freezing schemes respectivey. Here, tendency is defined as the contribution of a particular process to the change in the given prognostic variable within a time step.

It was found that the model tended to produce most of the ice near to cloud top which then quickly grew to form snow (and subsequently graupel), which were then removed by sedimentation. This removal of ice at cloud top allows conditions for fresh ice to form subsequently. Cloud top temperature (ignoring any cloud above 4 km to focus on shallow cloud) was not found to change significantly from run to run. However, a significant fraction of the simulated shallow convective cloud exhibited temperatures below −10 °C at cloud top, with some localised turrets approaching −14 °C, which is significantly colder than that inferred from MODIS (Moderate Resolution Imaging Spectroradiometer) satellite retrievals concurrent with the sampling period, CFARR radar and aircraft observations at cloud top. In terms of the ice concentration tendencies, the Cooper parameterization was seen to produce the larger of the two contributions, both in terms of magnitude and spatial extent. However it is interesting to note that when both the Cooper and freezing schemes were switched on together as part of the same simulation, the contribution from the Cooper scheme was reduced considerably due to competition with the droplet-freezing scheme. However given that cloud top temperature is colder in the model than in reality, in any given configuration the schemes will most likely produce slightly more primary ice, a problem which is exacerbated by the ability of the model to regenerate small amounts of fresh ice at each time-step. This result serves as a useful illustration of the outstanding issues and challenges that exist when representing shallow convection in current mesoscale models, particularly in

ACPD
11, 30797–30851, 2011

terms of the importance of cloud macrostructure and how errors in the meteorological conditions can influence the microphysics.

2.5 Sensitivity studies of the HM Mechanism using ACPIM

To expand on the WRF study, a 1-D column process model with bin microphysics was used to further explore the microphysical processes occurring within the cloud. The scheme used is the Aerosol Cloud and Precipitation Interactions Model (ACPIM), developed at the University of Manchester (detailed in Dearden et al., 2011). In the model, aerosols and water particles are represented by having a 2-D grid representing the number concentration of aerosols of mass m_a and associated water mass m_w, as described by Bott (2000). This allows a spectrum of particles with different aerosol mass to be formed from the subsequent collision of activated droplets. The aerosol size distribution can be input to the model where the aerosols are assumed to be in equilibrium with the ambient humidity below cloud base and their water content is derived using the Zdanovskii-Stokes-Robinson (ZSR) mixing rule (Stokes and Robinson, 1966). The aerosols grow according to the droplet growth equation (Pruppacher and Klett, 1997) with a condensation coefficient of 1 and thermal accommodation coefficient of 0.7. They are transferred along the bin grid using the moving centre bin scheme (Jacobson, 2005); other bin schemes have been trialled, including single moment Kovetz and Olund (1969) and the 2-moment hybrid bin scheme (Chen and Lamb, 1994b) but we use the moving centre scheme here due to its simplicity and low numerical diffusion. The droplets grow along Kohler curves that are defined from the ZSR mixing rule and the Kelvin equation, using a surface tension equal to that of pure water (Topping et al., 2005); we also utilise ventilation coefficients for heat and vapour, Pruppacher and Klett (1997). Once activated the drops grow by collision and coalescence with the gravitational kernel adapted from Hall (1980). The numerical scheme used to solve the stochastic coalescence equation is a 2-moment scheme conserving number and mass. The ice nucleation scheme described by DeMott et al. (2010) is used to initiate ice in the model. This scheme requires a knowledge of the number of aerosols larger

ACPD
11, 30797–30851, 2011

than 0.5 µm diameter as input, which is diagnosed from the prognostic aerosol bins within the model. Once formed, ice crystals grow from the vapour using the variable aspect ratio, variable density model described by Chen and Lamb (1994a), where the aspect ratio tends towards an inherent growth ratio as observed in the experiments of Fukuta (1969). The variable density reflects the fact that hollow crystals are produced at high supersaturations due to rarefactions in the vapour field, whereas the inherent growth ratio reflects the changes in the deposition coefficients on the different crystallographic faces (Libbrecht, 2005). Crystals also grow by aggregation, and here an aggregation efficiency of 0.1, based on the laboratory experiments by Connolly et al. (2011) has been chosen, while riming efficiencies were set to unity. The size of aggregates of ice crystals is defined by using a fractal-like dimension of 2 such that ice crystal mass is proportional to particle diameter squared (Westbrook et al., 2004), and by specifying that the first aggregation occurs with the two major axes at a 45° angle, while riming serves to fill in the ice matrix until it forms an ice sphere, whereupon rime mass is deposited to form an ice shell of high density. During riming in the temperature range of −2.5 to −7.5 °C ice shards are ejected at a rate equal to 350 splinters per kg of air per milligram of rime accreted (Hallett and Mossop, 1974).

The calculations carried out by this idealised model can only be taken in a relative sense as the dynamical framework is somewhat unrealistic; nevertheless there is value in doing this as the cloud system in this case study persisted for several hours. It is assumed that ice is formed by primary nucleation and falls against the updraft, but is mostly levitated by the updraft, whereas liquid water is supplied through condensation, which occurs as the air is lifted by the updraft. In this investigation the parcel was lifted at ∼0.5 ms^{-1} (based on typical values observed by the lidar) until it reached the −5 °C level, following which the ascent of the parcel was terminated. Initial conditions for the parcel were: RH = 95 %, T = +1 °C, P = 950 mbar. This leaves the simulation with the correct liquid water content (for an undiluted parcel) with ice crystals formed by primary nucleation and growth occurring by vapour deposition, riming and aggregation. Note that the model does not distinguish between cloud drops and warm rain per se, but

ACPD
11, 30797–30851, 2011

adopts the convention that drops larger than 80 µm diameter are classified as rain and those smaller are cloud particles (Seifert and Beheng, 2006).

In order to assess the sensitivity to IN number the model was run as described, however, the primary ice nucleation scheme was altered by shifting the temperature used as input to the parameterisation by ΔT=0, −2, −4, −6, −8 °C. For these five runs, the sensitivity to the input aerosol population was tested. One set of runs was performed using the aerosol observed at the ground at CFARR as input, approximated by three lognormal modes fitted to the size distribution (see Fig. 6). This is referred to as the "high" aerosol input case. Another set of runs used the above but with a reduced total aerosol number in the main accumulation mode, lognormal distribution (by a factor of six) was used while maintaining the shape of the distribution and keeping the larger mode the same so that the number of IN was constant (referred to as "low" aerosol input). All simulations lasted 3 h, of the order of the observed cloud lifetime. These runs were also performed with the Hallett-Mossop process both "on" and "off". Due to the insensitivity of the runs with the "high" aerosol input to the HM process we only report the runs with HM "on" for those cases. In total 5 runs for the "high" aerosol input, and 10 runs (HM "on" and "off") for the "low" aerosol input were performed.

2.5.1 ACPIM Parcel Model Results

We now present one of the ACPIM model runs in detail to aid a discussion and interpretation of the microphysical processes occurring within the observed cloud, before providing a summary of all the simulations. Figure 12 shows the water contents predicted by ACPIM as a function of time for the model run where the temperature input to the DeMott scheme was shifted by 8 °C to lower temperatures, and the low aerosol input was reduced to 1/6th of the concentration measured at the ground. It can be seen that the modelled liquid water content agrees approximately with the maximum water content measured in the cloud (~1 g m^{-3}). It takes ~10 min, after peak LWC is achieved, for warm rain to develop (at 40 min) and a further 10 min (at 50 min) for

ACPD
11, 30797–30851, 2011

this rain to reach a significant fraction of the total water content. At 60 min, the warm rain starts to capture some of the crystals produced by primary nucleation and freezes to form large, effective, riming particles. Note that at this point the rain water content ($0.4\,g\,m^{-3}$) is consistent with observed peak values along run 3 (Fig. 5). This is the point where the ice crystal mass (Fig. 12) and number concentration (Fig. 13) starts to increase rapidly, eventually approaching values observed by the aircraft of $\sim 1\,g\,m^{-3}$ and $\sim 100\,L^{-1}$ respectively. 100 minutes into the simulation the cloud completely glaciates. Note that the ice crystal concentration decreases by the end of the simulation due to aggregation, to ~ few 10's per litre. The aircraft ice particle imagery data also showed an increase in the concentration of aggregated particles at times, along with a reduction in total ice particle concentrations.

The droplet number concentration within the model ($\sim 90\,cm^{-3}$) is in reasonable agreement with the data; however, this is sensitive to the aerosol dilution factor, which is uncertain and therefore this does not represent per se a complete test of the aerosol activation mechanism within the model. Regions with the highest observed concentrations of ice in run 3 tend to be those with very few drops that are close to complete glaciation. This is well reproduced with the model. An interesting finding from the model is that roughly half of the ice mass is due to riming (Fig. 12).

Figure 14 (left) shows a summary of all the model runs completed, presented as maximum ice concentrations for the different temperature shifts input to the DeMott parameterisation. It is evident that the runs with "low" aerosol input and HM switched on have, produced by far the highest ice crystal concentrations (by 3–4 orders of magnitude). In runs with "high" aerosol input the predicted drop number concentration was $\sim 450\,cm^{-3}$ which meant the warm rain process was not active, so no effective rimers were present to initiate secondary ice by rime-splintering. Indeed, the ice crystal concentration in the case with HM switched off was almost exactly the same (c.f. dashed and dashed-dot lines). Surprisingly, the maximum ice concentration in runs with an active HM process is relatively insensitive to the initial number of primary ice crystals. Note the small difference between the high aerosol with HM case and low aerosol

ACPD
11, 30797–30851, 2011

without HM case. This is due to the fact that there are more aerosols larger than 0.5 µm in the high aerosol case, rather than any HM process.

Figure 14 (right) shows the time-taken to reach ice concentrations of $\sim 100\,L^{-1}$ for the different temperature shifts for the DeMott scheme. It shows that this time-scale is highly sensitive to the initial number of primary ice nuclei and thus highlights the continued importance of better quantifying primary ice nuclei concentrations at these high temperatures.

3 Source of the primary ice nuclei

The DeMott et al. (2010) parameterisation does not implicitly specify the ice nuclei type at these high temperatures, but we may gain some insight from the surface aerosol measurements since it has been demonstrated from the aircraft in situ and remote sensing measurements that there is coupling between the air at the ground and the air just below the inversion (i.e. just below cloud base), and hence with the air entering cloud. Using the ice nuclei surface area dependent active sites concept described in Connolly et al. (2009), (M. Niemand et al., personal communication, 2011) have investigated a range of mineral dusts and found that the surface site density shows a similar dependence for all of the dusts investigated at temperatures lower than −10 °C. At −10 °C the aerosol surface site density, n_s is $\sim 1\times10^6\,m^{-2}$ and increases as T decreases, and so if extrapolated to T >-10°C suggests a decrease in surface active site density would be likely. From Fig. 6 it can be seen that $\sim 1\,cm^{-3}$ of the observed particles were mineral dust in origin as determined by the EDX analysis. We estimate the number of these particles that would act as ice nuclei, N_{ice}, at a given temperature, T, as follows:

$$N_{ice} = \int_0^{D_{max}} \frac{dN(D)}{dD} \times \left(1 - \exp\left[-\frac{\pi D^2}{4} \times n_s\{T\}\right]\right) dD \quad (1)$$

ACPD
11, 30797–30851, 2011

where n_s is the number of ice active sites per unit area of a dust particle (as a function of temperature) and D is the diameter of the aerosol particle (for simplicity particles are assumed to be spherical in this case). A full description of the derivation is provided in Connolly et al. (2009) (see Eq. 9 of that paper).

Applying Eq. (1) to the observed aerosol properties, Fig. 6, yields a primary ice crystal concentration due to mineral dust nucleation of no larger than $\sim 1 \times 10^{-3}\,L^{-1}$, at the current warm temperature limit of the relationship (which is $-10^{\circ}C$). Extrapolating to $-5^{\circ}C$ suggests concentrations should be at most $\sim 1 \times 10^{-4}\,L^{-1}$. This value is also likely to be significantly lower, by the factor of 1/6, as previously discussed, due to the effects of the entrainment limitation through the inversion. It is worth noting that the DeMott parameterisation for these data yields concentrations between 1×10^{-2} and $1 \times 10^{-1}\,L^{-1}$ (see Fig. 14 for the case without an active HM process). Clearly the concentrations of ice particles due to mineral dust activation alone are not sufficient, in this particular case, to explain the observed concentrations.

Biological particle size distributions ($0.5 < D_p < 20\,\mu m$) were also measured at the surface site (see Fig. 6) using the WIBS instrument. In order to estimate the concentrations of ice nuclei due to these particles we assume (in this environment) that fluorescent particles with diameter less than $\sim 10\,\mu m$ in diameter were of mainly single bacteria, bacterial clumps or small spores, while those greater than $10\,\mu m$ were mainly pollen (e.g. Burrows et al. (2009)). We then use available literature to estimate their activity in the freezing mode. Diehl et al. (2006) parameterised ice nucleation on bacteria, pollen and mineral dusts using the following equation;

$$\frac{dN}{dt} = N_u a B V_d \exp(aT_c)\frac{dT}{dt} \tag{2}$$

where a ($^{\circ}C^{-1}$) and B (cm^{-3}), are are constants derived from laboratory data. The quantity:

$$aBV_d \exp(aT_c) \tag{3}$$

ACPD
11, 30797–30851, 2011

represents the number of active ice nuclei, that become active per unit temperature interval, within a droplet of volume V_d at temperature T_c, whereas:

$$BV_d \exp(aT_c) \quad (4)$$

represents the number of ice nuclei active in the same drop at temperature T_c. Table 1 of Diehl et al. (2006), lists values of B for different particle types, which for bacteria and pollen are $B = 6.19\,\mathrm{cm}^{-3}$ and $1.01 \times 10^{-2}\,\mathrm{cm}^{-3}$ respectively. The results for bacteria are derived from Levin and Yankofsky (1983), while for pollen they are derived from the study of Diehl et al. (2002).

In Levin and Yankofsky's study drop sizes were reported to be 1 mm and the number of bacteria particles per drop was $5\mathrm{x}10^5$. Levin and Yankofsky reported that ~50 % of drops were active at −5°C, which means effectively 1 in 1 million bacteria can be active as an ice nucleus. At −10°C, 100 % were active i.e. the ice active fraction was 2 in 1 million. The WIBS reported concentrations of biological particles of ~0.1 cm^{-3} during the aircraft flights (D_p <10 µm) and hence the ice active number concentration is $\sim 1 \times 10^{-4}\,\mathrm{L}^{-1}$, which is similar to the mineral dust concentrations. This assumes that one biological "particle" will consist of, or carry, a single bacterium (rather than having several bacteria or clumps of bacteria per particle). This is a reasonable assumption when considering the typical size of a bacterium (a few microns) which is comparable to the size of the observed aerosol.

In the study by Diehl et al. (2002), their prepared laboratory mixtures contained 35 mg of pollen per 100 ml of water and it was stated that pollen sizes were between 25 and 75 microns. Pollen particle densities are typically $1200\,\mathrm{kg\,m}^{-3}$ (e.g. in Gregory (1973)) thus assuming a diameter of 50 µm, this equates to a pollen concentration of $\sim 4.5 \times 10^9\,\mathrm{m}^{-3}$ per droplet. The drop diameters quoted were between 500 to 750 µm, so pollen numbers per drop would have been between 0.3 (for 500 µ drops) and 1 (for 750 µm drops). At −5°C the number of ice nuclei in the same drops, calculated using the B parameter quoted above would be between 1×10^{-4} and 3×10^{-4}, so the ice active fraction in each case is $\sim 3 \times 10^{-4}$. The fact that both drop size calculations yield

ACPD
11, 30797–30851, 2011

the same active fraction strongly suggests that it is more appropriate to parameterise ice nucleation based on the number of particles within the drops rather than using the drop volume, as in Diehl et al. (2006). Our reason for doing this is that we assume, in this case, that the biological particles will be scavenged by cloud activation, so that a cloud droplet only contains one biological particle (i.e. we have assumed nucleation scavenging is dominant). Most pollen particles range in size from 15–40 µm diameter, although some can be as small as 10 µm, whilst fragments of pollen between 0.5–4 µm (so-called sub-pollen particles) can also be present (Bacsi et al., 2006). Strictly we cannot assume that the ∼0.1 cm^{-3} of biological particles are pollen, but if we do then the concentration of ice nuclei would be 0.03 L^{-1} at -5°C or 0.67 L^{-1} at −8 °C.

Further to these arguments it was found by Möhler et al. (2008) that pseudomonas Syringae bacteria were active as ice nuclei at −8 °C and could account for IN concentrations of around 0.01 L^{-1} although we do not have any measurements specific to this species of bacteria. Further, Conen et al. (2011) found that soil particles which consisted of a mixture of mineral and biological material were sometimes able to act as ice nuclei at temperatures as high as −7 °C

While inconclusive, due to the lack of aircraft insitu biological particle data, calculations based on reasonable extrapolations of laboratory data and the observed bioaerosol concentrations at the surface, allow us to conclude that it is entirely plausible that a significant fraction of the primary ice nuclei at the observed temperatures were likely of biological origin.

4 The Hallett-Mossop secondary production mechanism

All of the in-situ observations performed during this study displayed enhanced ice crystal number concentrations that cannot be explained by primary nucleation alone. Calculated vertical profiles of predicted ice nuclei number concentrations in the observation region predict maximum values of ∼0.1 L^{-1} for the DeMott scheme and 1.2 L^{-1} for the Meyers scheme. However, the in-situ microphysical observations revealed regions

ACPD
11, 30797–30851, 2011

of cloud which contained over an order of magnitude more ice than can be predicted using either scheme. In the regions of enhanced ice number concentrations, 2DS images displayed a significant number of small columnar crystals coexisting with droplets and graupel suggesting secondary ice production via the Hallett-Mossop rime splintering process was occurring. To test this, Eq. (1) of Harris-Hobbs and Cooper (1987) was applied to the data using the approach described by Crosier et al. (2011). First an "observed" splinter production rate was computed using the ice particle size distribution observed within the HM zone (Run R3, 34 km from CFARR) which displayed a small mode of columns with sizes ranging from 45 to 145 µm in length. Assuming an ice crystal growth rate of 0.4 µm s^{-1} at −3.5 °C (e.g. Ryan et al. (1976)) this would equate to an elapsed time of 250 s to allow the crystals to grow across the size range observed, under steady state, water saturated conditions. This implies a required splinter production rate of ∼80 m^{-3} s^{-1} in order to maintain the observed crystal concentrations.

The Harris-Hobbs and Cooper equations were then used to predict a splinter production rate using the observed cloud droplet size distribution from run R1 as being representative of the supercooled droplet distribution observed below the HM boundary. The 2DS ice size distributions from run R3 (35.1 km – 33.6 km from CFARR) were used as representative of the riming ice distribution. For a droplet-ice collection efficiency of 1.0, the predicted splinter production rate was calculated to be 40.2 m^{-3} s^{-1}. Applying the droplet-ice collection efficiency of Beard and Grover (1974) reduced this production rate to 28.8 $m^{-3}s^{-1}$. These results cannot quite be reconciled with the "observed" splinter production rate. We therefore examined the effect of relaxing the condition that requires large droplets (D > 24 µm) to be present to enable splinter production to occur as they rime. Reducing the large droplet limit to D > 22 µm yielded a production rate of 120 m^{-3} s^{-1} (72.7 m^{-3} s^{-1} with the B&G collection efficiency), whilst a further reduction to D > 20 µm gave a predicted rate of 320 m^{-3} s^{-1} (200 m^{-3} s^{-1} with B&G), which is too large a rate. Clearly relaxing the large droplet constraint improves the agreement between the observed and predicted splinter production rates, which is consistent with the results of Crosier et al. (2011). Reducing the critical drop size may not be an

ACPD
11, 30797–30851, 2011

unreasonable step to take; laboratory experiments by Choularton et al. (1978, 1980) showed photographic evidence for protuberances occurring on droplets as small as 10 and 15 µm in diameter, suggesting that small droplets can undergo symmetrical freezing to create an ice shell, which may subsequently fracture and produce splinters. However, this also highlights the accuracy which airborne instrumentation must achieve for absolute size measurements of droplets, particularly in mixed phase conditions, i.e. to significantly better resolution than 2 µm, in order to investigate secondary ice processes. Laboratory studies are planned to further investigate and refine this aspect of the Hallett-Mossop process.

5 Summary of model results

A combined modelling and observation study was used to investigate the role of the Hallett-Mossop secondary ice production process in terms of its influence on precipitation from a winter-time shallow convective cloud region over the southern part of the UK. Whilst the WRF model results showed some increase in the spatial extent of precipitation occurrence due to inclusion of the Hallett-Mossop process, the treatment of primary ice nucleation was found to have the most significant control on precipitation, at least in this particular case. The WRF model was able to reproduce total ice number concentrations of several per litre even in the absence of the Hallett-Mossop process, which was sufficient to sustain precipitation as the convective cells were advected eastwards towards the Chilbolton region. However, it was only able to reproduce these high concentrations of primary ice particles due to the fact that cloud tops in the model achieved lower temperatures than were actually observed, effectively reducing the model sensitivity to the HM process. This was due to the inability of the model to capture the temperature inversion observed at 2 km. The problem generated by this serves to highlight the difficulties encountered when using mesoscale models to simulate slightly supercooled shallow convective clouds common to the UK.

ACPD
11, 30797–30851, 2011

The ACPIM studies in particular found the HM process to be a powerful mechanism for ice production, yielding 3 orders of magnitude more ice than predicted by the DeMott el al. (2010) primary scheme acting alone. However, typical timescales of ∼20 min were required to produce ice concentrations approaching those observed, even when the concentrations of primary ice were equal to those expected for a cloud top temperature of −13 °C, some 6°C colder than was observed. In these simulations the time taken to reach peak ice crystal concentrations was found to be dependent on the temperature assumed in the DeMott et al. (2010) parameterisation. This sensitivity analysis was undertaken in order to match the predicted ice nuclei with the observed ice crystal concentrations. This underlines the importance of better quantifying the number of active ice nuclei present at these higher temperatures. Also highlighted is the importance of accurately measuring the cloud top temperature as well as identifying which particles are able to act as ice nuclei at temperatures as warm as −7 °C. Chamber studies suggest that dust particles are ineffective at these temperatures, however, in this study WIBS measurements indicated that a significant number of particles in the boundary layer, were very likely biological in origin. If only a small fraction of these entered cloud and were effective as ice nuclei then this could account for the observed primary ice nucleation required to initiate the secondary ice particle production observed. Without any available cloud particle residual measurements, or airborne bioaerosol measurements, however, this cannot be confirmed.

Finally, ACPIM runs with "high" aerosol number concentrations and thus high droplet concentrations, showed no evidence of ice enhancement over primary ice concentrations. This was as a result of the inability to grow drops of sufficient size in these conditions which could then precipitate through the cloud collecting primary ice particles to form the instant rimer particles required to initiate the HM splinter production process. This highlights the importance of warm rain production to this secondary ice particle production mechanism (Jameson et al., 1996).

ACPD
11, 30797–30851, 2011

6 Conclusions

The coupled high-resolution ground, remote sensing and aircraft observations of convective clouds we present here highlight cases close to the so-called ice "multiplication boundary" described by Mossop (1978). The multiplication boundary is defined by the cloud-base temperature, temperature profile and droplet number concentration that determines whether HM multiplication can or cannot proceed effectively. We have investigated this region in detail and show how measured aerosol properties below cloud base can, with care, be used to model and interpret the subsequent microphysical processes occurring within such shallow convective clouds. We have also shown the difficulty in reconciling "observed" and calculated splinter production rates unless the Hallett-Mossop droplet freezing criterion is relaxed. We applied the WRF and ACPIM models to reveal how the ice phase and precipitation within aged, slightly supercooled cumulus cloud systems develop, and looked at the influence both the HM process and primary ice nucleation mechanisms have on these. The results emphasise the importance of and sensitivity to primary ice nucleation, and the need for accurate ice nuclei concentration measurements as well as the characterisation of these particles. For example: (1) the observed glaciation of the cloud could only be simulated using current ice nucleation schemes if the modelled cloud top was colder than actually observed (or the schemes were simply provided with prescribed temperatures lower than were observed); (2) Significant ice nucleation was required at $-7\,^{\circ}C$ and this could plausibly be accounted for by the presence of efficient warm temperature ice nuclei, e.g. biological, particles, entering cloud, significant concentrations of which were observed at the ground. The power of secondary ice particle production by the Hallett-Mossop process in producing large numbers of ice crystals at temperatures around -6°C emphasises the need to understand ice nucleation in slightly supercooled clouds even though the number of ice particles produced may be small.

WRF model simulations found the precipitation efficiency of the cloud was not strongly sensitive to secondary ice via the Hallett-Mossop process since ice formed by

ACPD
11, 30797–30851, 2011

primary nucleation was able to produce the intensity of precipitation observed. Including secondary ice processes however does modify the spatial distribution of simulated precipitation in the WRF model. The ACPIM results also highlight the importance of warm rain in the Hallett-Mossop process, where rain drops, once formed, are able to capture ice crystals to produce effective rimers which then participate in secondary ice multiplication processes and rapid cloud glaciation, at least within thermodynamically favourable cloud regions. This process creates a chain reaction (Phillips, 2001), leading to enhanced numbers of ice crystals, as observed in these cases. It is suggested, based on these results, that further laboratory studies of the HM process are required to validate the suggested relaxation in the droplet freezing criteria.

Acknowledgements. This work was funded by the NERC APPRAISE programme, grant number NE/E01125X/1. Christopher Dearden was funded by NERC studentship NE/F00821X/1 in a case award with the Met Office. We would like to acknowledge the support from FGAM, FAAM and Direct Flight in obtaining the aircraft dataset. We would also like to thank the following for supporting the CFARR measurements: Andrew Barrett (University of Reading), Darcy Ladd and Charles Wrench (CFARR). MODIS data were obtained from the NASA LAADS online archive (http://ladsweb.nascom.nasa.gov/). Coastline data were obtained from the online NOAA coastline extractor (http://rimmer.ngdc.noaa.gov/). Surface pressure fields were obtained from the ECMWF Interim Re-Analysis archive (http://data.ecmwf.int/data/). Radiosonde data were obtained from the University of Wyoming Sounding Archive (http://weather.uwyo.edu/upperair/sounding.html).

References

Ansmann, A., Tesche, M., Althausen, D., Müller, D., Seifert, P., Freudenthaler, V., Heese, B., Wiegner, M., Pisani, G., Knippertz, P., and Dubovik, O.: Influence of Saharan dust on cloud glaciation in southern Morocco during the Saharan Mineral Dust Experiment, J. Geophys. Res., 113, D04210, doi:10.1029/2007JD008785, 2008. 30800

Bacsi, A., Choudhury, B. K., Dharajiya, N., Sur, S., and Boldogh, I.: Subpollen particles: carriers of allergenic proteins and oxidases, The J. Allergy Clin. Immun., 118, 844–50, doi:10.1016/j.jaci.2006.07.006, 2006. 30825

ACPD

11, 30797–30851, 2011

Bigg, E. K.: The formation of atmospheric ice crystals by the freezing of droplets, Q. J. Roy. Meteor. Soc., 79, 510–519, doi:10.1002/qj.49707934207, 1953. 30816
Blyth, A. M. and Latham, J.: Development of ice and precipitation in New Mexican summertime cumulus clouds, Q. J. Roy. Meteor. Soc., 119, 91–120, doi:10.1002/qj.49711950905, 1993. 30801
Bott, A.: A Flux Method for the Numerical Solution of the Stochastic Collection Equation: Extension to Two-Dimensional Particle Distributions, J. Atmos. Sci., 57, 284–294, doi:10.1175/1520-0469(2000)057<0284:AFMFTN>2.0.CO;2, 2000. 30818
Bouniol, D., Illingworth, A. J., and Hogan, R. J.: Deriving turbulent kinetic energy dissipation rate within clouds using ground based 94 GHz radar, in: 31st AMS conference on Radar Meteorology, 2003. 30809
Bower, K., Moss, S., Johnson, D., Choularton, T., Latham, J., Brown, R., Blyth, A., and Cardwell, J.: A parametrization of the ice water content observed in frontal and convective clouds, Q. J. Roy. Meteor. Soc., 122, 1815–1844, 1996. 30801
Burrows, S. M., Butler, T., Jöckel, P., Tost, H., Kerkweg, A., Pöschl, U., and Lawrence, M. G.: Bacteria in the global atmosphere – Part 2: Modeling of emissions and transport between different ecosystems, Atmos. Chem. Phys., 9, 9281–9297, doi:10.5194/acp-9-9281-2009, 2009. 30823
Chen, J.-P. and Lamb, D.: The Theoretical Basis for the Parameterization of Ice Crystal Habits: Growth by Vapor Deposition, J. Atmos. Sci., 51, 1206–1222, doi:10.1175/1520-0469(1994)051<1206:TTBFTP>2.0.CO;2, 1994a. 30819
Chen, J.-P. and Lamb, D.: Simulation of Cloud Microphysical and Chemical Processes Using a Multicomponent Framework. Part I: Description of the Microphysical Model, J. Atmos. Sci., 51, 2613–2630, doi:10.1175/1520-0469(1994)051<2613:SOCMAC>2.0.CO;2, 1994b. 30818
Choularton, T. W., Latham, J., and Mason, B. J.: A possible mechanism of ice splinter production during riming, Nature, 274, 791–792, doi:10.1038/274791a0, 1978. 30827
Choularton, T. W., Griggs, D. J., Humood, B. Y., and Latham, J.: Laboratory studies of riming, and its relation to ice splinter production, Q. J. Roy. Meteor. Soc., 106, 367–374, doi:10.1002/qj.49710644809, 1980. 30827
Conen, F., Morris, C. E., Leifeld, J., Yakutin, M. V., and Alewell, C.: Biological residues define the ice nucleation properties of soil dust, Atmos. Chem. Phys., 11, 9643–9648, doi:10.5194/acp-11-9643-2011, 2011. 30825

ACPD
11, 30797–30851, 2011

Connolly, P. J., Möhler, O., Field, P. R., Saathoff, H., Burgess, R., Choularton, T., and Gallagher, M.: Studies of heterogeneous freezing by three different desert dust samples, Atmos. Chem. Phys., 9, 2805–2824, doi:10.5194/acp-9-2805-2009, 2009. 30800, 30809, 30822, 30823

Connolly, P. J., Emersic, C., and Field, P. R.: A laboratory investigation into the aggregation efficiency of small ice crystals, Atmos. Chem. Phys. Discuss., 11, 25655–25707, doi:10.5194/acpd-11-25655-2011, 2011. 30819

Cooper, W.: Ice initiation in natural clouds. Precipitation enhancement: A Scientific Challenge, Am. Meteorol. Soc., 43, 29–32, 1986. 30816

Crosier, J., Bower, K. N., Choularton, T. W., Westbrook, C. D., Connolly, P. J., Cui, Z. Q., Crawford, I. P., Capes, G. L., Coe, H., Dorsey, J. R., Williams, P. I., Illingworth, A. J., Gallagher, M. W., and Blyth, A. M.: Observations of ice multiplication in a weakly convective cell embedded in supercooled mid-level stratus, Atmos. Chem. Phys., 11, 257–273, doi:10.5194/acp-11-257-2011, 2011. 30801, 30804, 30826

Dearden, C., Connolly, P. J., Choularton, T. W., and Field, P. R.: Evaluating the effects of microphysical complexity in idealised simulations of trade wind cumulus using the Factorial Method, Atmos. Chem. Phys., 11, 2729–2746, doi:10.5194/acp-11-2729-2011, 2011. 30818

DeMott, P. J., Sassen, K., Poellot, M. R., Baumgardner, D., Rogers, D. C., Brooks, S. D., Prenni, A. J., and Kreidenweis, S. M.: African dust aerosols as atmospheric ice nuclei, Geophys. Res. Lett., 30, 1732, doi:10.1029/2003GL017410, 2003. 30801

DeMott, P. J., Prenni, A. J., Liu, X., Kreidenweis, S. M., Petters, M. D., Twohy, C. H., Richardson, M. S., Eidhammer, T., and Rogers, D. C.: Predicting global atmospheric ice nuclei distributions and their impacts on climate., P. Natl. Acad. Sci. USA, 107, 11217–11222, doi:10.1073/pnas.0910818107, 2010. 30800, 30801, 30818, 30822, 30851

Diehl, K., Matthias-Maser, S., Jaenicke, R., and Mitra, S. K.: The ice nucleating ability of pollen:: Part II. Laboratory studies in immersion and contact freezing modes, Atmos. Res., 61, 125–133, 2002. 30824

Diehl, K., Simmel, M., and Wurzler, S.: Numerical sensitivity studies on the impact of aerosol properties and drop freezing modes on the glaciation, microphysics, and dynamics of clouds, J. Geophys. Res., 111, D07202, doi:10.1029/2005JD005884, 2006. 30823, 30824, 30825

Forster, P., Ramaswamy, V., Artaxo, P., Berntsen, T., Betts, R., Fahey, D., Haywood, J., Lean, J., Lowe, D., Myhre, G., Nganga, J., Prinn, R., Raga, G., Schulz, M., and Van Dorland, R.: Changes in Atmospheric Constituents and in Radiative Forcing, in: Climate Change 2007: The Physical Science Basis. Contribution of Working Group I to the Fourth Assessment

ACPD
11, 30797–30851, 2011

Report of the Intergovernmental Panel on Climate Change, Cambridge University Press, 2007. 30799

Fukuta, N.: Experimental Studies on the Growth of Small Ice Crystals, J. Atmos. Sci., 26, 522–531, doi:10.1175/1520-0469(1969)026<0522:ESOTGO>2.0.CO;2, 1969. 30819

Gabey, A. M., Gallagher, M. W., Whitehead, J., Dorsey, J. R., Kaye, P. H., and Stanley, W. R.: Measurements and comparison of primary biological aerosol above and below a tropical forest canopy using a dual channel fluorescence spectrometer, Atmos. Chem. Phys., 10, 4453–4466, doi:10.5194/acp-10-4453-2010, 2010. 30809

Goddard, J. W. F., Eastment, J. D., and Thurai, M.: The Chilbolton advanced meteorological radar: a tool for multidisciplinary atmospheric research, Electron. Commun. Eng., 6, 77–86, 1994. 30802

Gregory, P.: The microbiology of the atmosphere, New York, Interscience Publishers, 2nd edn., 1973. 30824

Hall, W. D.: A Detailed Microphysical Model Within a Two-Dimensional Dynamic Framework: Model Description and Preliminary Results, J. Atmos. Sci., 37, 2486–2507, doi:10.1175/1520-0469(1980)037<2486:ADMMWA>2.0.CO;2, 1980. 30818

Hallett, J. and Mossop, S. C.: Production of secondary ice particles during the riming process, Nature, 249, 26–28, 1974. 30801, 30819

Harris-Hobbs, R. L. and Cooper, W. A.: Field Evidence Supporting Quantitative Predictions of Secondary Ice Production Rates, J. Atmos. Sci., 44, 1071–1082, doi:10.1175/1520-0469(1987)044<1071:FESQPO>2.0.CO;2, 1987. 30826

Hogan, R. J., Field, P. R., Illingworth, A. J., Cotton, R. J., and Choularton, T. W.: Properties of embedded convection in warm-frontal mixed-phase cloud from aircraft and polarimetric radar, Q. J. Roy. Meteor. Soc., 128, 451–476, doi:10.1256/003590002321042054, 2002. 30801

Huang, X.-Y., Xiao, Q., Barker, D. M., Zhang, X., Michalakes, J., Huang, W., Henderson, T., Bray, J., Chen, Y., Ma, Z., Dudhia, J., Guo, Y., Zhang, X., Won, D.-J., Lin, H.-C., and Kuo, Y.-H.: Four-Dimensional Variational Data Assimilation for WRF: Formulation and Preliminary Results, Mon. Weather Rev., 137, 299–314, doi:10.1175/2008MWR2577.1, 2009. 30801

Illingworth, A. J., Hogan, R. J., O'Connor, E. J., Bouniol, D., Delanoë, J., Pelon, J., Protat, A., Brooks, M. E., Gaussiat, N., Wilson, D. R., Donovan, D. P., Baltink, H. K., van Zadelhoff, G.-J., Eastment, J. D., Goddard, J. W. F., Wrench, C. L., Haeffelin, M., Krasnov, O. A., Russchenberg, H. W. J., Piriou, J.-M., Vinit, F., Seifert, A., Tompkins, A. M., and Willén,

ACPD
11, 30797–30851, 2011

U.: Cloudnet – Continuous Evaluation of Cloud Profiles in Seven Operational Models Using Ground-Based Observations, B. Am. Meteorol. Soc., 88, 883–898, doi:10.1175/BAMS-88-6-883, 2007. 30802

Jacobson, M.: Fundamentals of Atmospheric Modeling, Cambridge University Press, New York, 2nd edn., doi:10.2277/0521548659, 2005. 30818

Jameson, A. R., Murphy, M. J., and Krider, E. P.: Multiple-Parameter Radar Observations of Isolated Florida Thunderstorms during the Onset of Electrification, J. Appl. Meteorol., 35, 343–354, doi:10.1175/1520-0450(1996)035<0343:MPROOI>2.0.CO;2, 1996. 30828

Kaye, P., Stanley, W. R., Hirst, E., Foot, E. V., Baxter, K. L., and Barrington, S. J.: Single particle multichannel bio-aerosol fluorescence sensor, Opt. Express, 13, 3583–3593, 2005. 30809

Kovetz, A. and Olund, B.: The Effect of Coalescence and Condensation on Rain Formation in a Cloud of Finite Vertical Extent, J. Atmos. Sci., 26, 1060–1065, doi:10.1175/1520-0469(1969)026<1060:TEOCAC>2.0.CO;2, 1969. 30818

Lance, S., Brock, C. A., Rogers, D., and Gordon, J. A.: Water droplet calibration of the Cloud Droplet Probe (CDP) and in-flight performance in liquid, ice and mixed-phase clouds during ARCPAC, Atmos. Meas. Tech., 3, 1683–1706, doi:10.5194/amt-3-1683-2010, 2010. 30803

Lawson, R. P., OConnor, D., Zmarzly, P., Weaver, K., Baker, B., Mo, Q., and Jonsson, H.: The 2D-S (Stereo) Probe: Design and Preliminary Tests of a New Airborne, High-Speed, High-Resolution Particle Imaging Probe, J. Atmos. Ocean. Technol., 23, 1462–1477, doi:10.1175/JTECH1927.1, 2006. 30803

Levin, Z. and Yankofsky, S. A.: Contact Versus Immersion Freezing of Freely Suspended Droplets by Bacterial Ice Nuclei, J. Clim. Appl. Meteorol., 22, 1964–1966, doi:10.1175/1520-0450(1983)022<1964:CVIFOF>2.0.CO;2, 1983. 30824

Libbrecht, K. G.: The physics of snow crystals, http://stacks.iop.org/0034-4885/68/i=4/a=R03, 2005. 30819

Marshall, J. S. and Palmer, W. M. K.: The Distribution of raindrops with size, J. Meteorol., 5, 165–166, doi:10.1175/1520-0469(1948)005<0165:TDORWS>2.0.CO;2, 1948. 30813

McFarquhar, G. M., Um, J., Freer, M., Baumgardner, D., Kok, G. L., and Mace, G.: Importance of small ice crystals to cirrus properties: Observations from the Tropical Warm Pool International Cloud Experiment (TWP-ICE), Geophys. Res. Lett., 34, L13803, doi:10.1029/2007GL029865,2007. 30803

Meyers, M. P., DeMott, P. J., and Cotton, W. R.: New Primary Ice-Nucleation Parameterizations in an Explicit Cloud Model, J. Appl. Meteorol., 31, 708–721, 1992. 30801, 30816

ACPD
11, 30797–30851, 2011

Möhler, O., Georgakopoulos, D. G., Morris, C. E., Benz, S., Ebert, V., Hunsmann, S., Saathoff, H., Schnaiter, M., and Wagner, R.: Heterogeneous ice nucleation activity of bacteria: new laboratory experiments at simulated cloud conditions, Biogeosciences, 5, 1425–1435, doi:10.5194/bg-5-1425-2008, 2008. 30825

Morcrette, C., Lean, H., Browning, K., Nicol, J., Roberts, N., Clark, P., Russell, A., and Blyth, A.: Combination of Mesoscale and Synoptic Mechanisms for Triggering an Isolated Thunderstorm: Observational Case Study of CSIP IOP 1, Mon. Weather Rev., 135, 3728–3749, doi:10.1175/2007MWR2067.1, 2007. 30806, 30812

Morrison, H., Curry, J. A., and Khvorostyanov, V. I.: A New Double-Moment Microphysics Parameterization for Application in Cloud and Climate Models. Part I: Description, J. Atmos. Sci., 62, 1665–1677, doi:10.1175/JAS3446.1, 2005. 30813

Mossop, S. C.: Some Factors Governing Ice Particle Multiplication in Cumulus Clouds, J. Atmos. Sci., 35, 2033–2037, doi:10.1175/1520-0469(1978)035<2033:SFGIPM>2.0.CO;2, 1978. 30801, 30802

Mossop, S. C., Cottis, R. E., and Bartlett, B. M.: Ice crystal concentrations in cumulus and stratocumulus clouds, Q. J. Roy. Meteorol. Soc., 98, 105–123, doi:10.1002/qj.49709841509, 1972. 30801

Penner, J., Andreae, M., Annegarn, H., Barrie, L., Feichter, J., Hegg, D., Jayaraman, A., Leaitch, R., Murphy, D., Nganga, J., and Pitari, G.: Climate Change 2001: The Scientific Basis: Chapter 6 Radiative Forcing of Climate Change, 2001. 30799

Phillips, V. T. J., DeMott, P. J., and Andronache, C.: An Empirical Parameterization of Heterogeneous Ice Nucleation for Multiple Chemical Species of Aerosol, J. Atmos. Sci., 65, 2757–2783, 2008. 30800

Pruppacher, H. and Klett, J.: Microphysics of Clouds and Precipitation, Kluwer Academic Publishers, Dordrecht, 2nd edn., 1997. 30818

Ryan, B. F., Wishart, E. R., and Shaw, D. E.: The Growth Rates and Densities of Ice Crystals between −3 °C and −21 °C, J. Atmos. Sci., 33, 842–850, doi:10.1175/1520-0469(1976)033<0842:TGRADO>2.0.CO;2, 1976. 30826

Sassen, K., DeMott, P. J., Prospero, J. M., and Poellot, M. R.: Saharan dust storms and indirect aerosol effects on clouds: CRYSTAL-FACE results, Geophys. Res. Lett., 30, 1633, doi:10.1029/2003GL017371, 2003. 30800

Saunders, C. P. R. and Hosseini, A. S.: A laboratory study of the effect of velocity on Hallett-Mossop ice crystal multiplication, Atmos. Res., 59–60, 3–14, 2001. 30802

ACPD
11, 30797–30851, 2011

Seifert, A. and Beheng, K. D.: A two-moment cloud microphysics parameterization for mixed-phase clouds. Part 1: Model description, Meteorol. Atmos. Phys., 92, 45–66, 2006. 30820
Stokes, R. H. and Robinson, R. A.: Interactions in Aqueous Nonelectrolyte Solutions. I. Solute-Solvent Equilibria, The Journal of Physical Chemistry, 70, 2126–2131, doi:10.1021/j100879a010, 1966. 30818
Topping, D. O., McFiggans, G. B., and Coe, H.: A curved multi-component aerosol hygroscopicity model framework: Part 2 –Including organic compounds, Atmos. Chem. Phys., 5, 1223–1242, doi:10.5194/acp-5-1223-2005, 2005. 30818
Ulbrich, I. M., Canagaratna, M. R., Zhang, Q., Worsnop, D. R., and Jimenez, J. L.: Interpretation of organic components from Positive Matrix Factorization of aerosol mass spectrometric data, Atmos. Chem. Phys., 9, 2891–2918, doi:10.5194/acp-9-2891-2009, 2009. 30809
Westbrook, C. D. and Illingworth, A. J.: Evidence that ice forms primarily in supercooled liquid clouds at temperatures > −27°C, Geophys. Res. Lett., 38, L14808, doi:10.1029/2011GL048021, 2011. 30800
Westbrook, C. D., Ball, R. C., Field, P. R., and Heymsfield, A. J.: Universality in snowflake aggregation, Geophys. Res. Lett., 31, L15104, doi:10.1029/2004GL020363, 2004. 30819
Whitby, K. T.: The physical characteristics of sulfur aerosols, Atmos. Environ. (1967), 12, 135–159, 1978. 30801

ACPD
11, 30797–30851, 2011

Table 1. Summary of constant altitude runs performed by the FAAM BAe146 aircraft in operational area to the west of Chilbolton on the 22 January 2009, flight reference B425. [a]Mean value from GPS receiver. [b]Mean value from de-iced Rosemount sensor.

Reference	Start Time (UTC)	End Time (UTC)	Altitude[a] (km)	Temperature[b]
R1	13:17:02	13:41:02	1.30	−1.0(± 0.1)
R2	13:43:00	13:52:09	0.75	3.7(± 0.3)
R3	13:56:07	14:15:21	1.26	−3.5(±0.3)
R4	14:16:45	14:29:14	1.93	−5.7(±0.3)
R5	14:32:33	14:50:59	2.24	−7.1(±0.3)
R6	14:50:59	15:03:40	2.54	−4.5(±0.4)
R7	15:04:49	15:23:32	2.20	−4.8(±0.1)

ACPD
11, 30797–30851, 2011

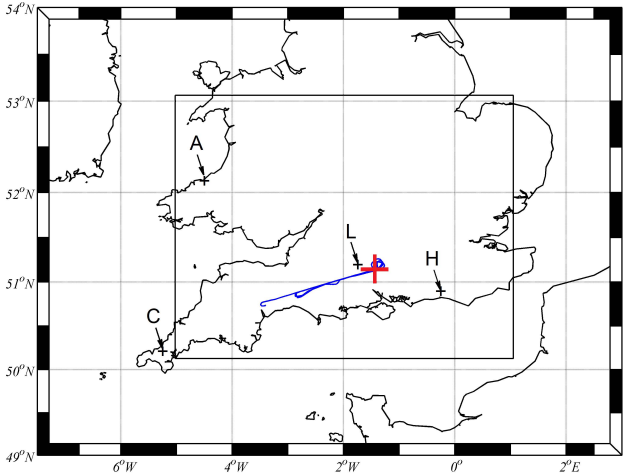

Fig. 1. 253 degree radial and flight track (blue) of the FAAM BAe146 aircraft on the 22 January 2009 (see Table 1 for details of runs/manoeuvres). Also shown are: the location of CFARR (red cross); the location of radiosonde stations at Cambourne, Larkhill, Herstmonceux and Aberporth (C, L, H and A respectively). The outer box relates to the 2nd domain used in the WRF model runs, while the inner box highlights the 3rd or inner domain used in the WRF model sensitivity studies (see text).

ACPD
11, 30797–30851, 2011

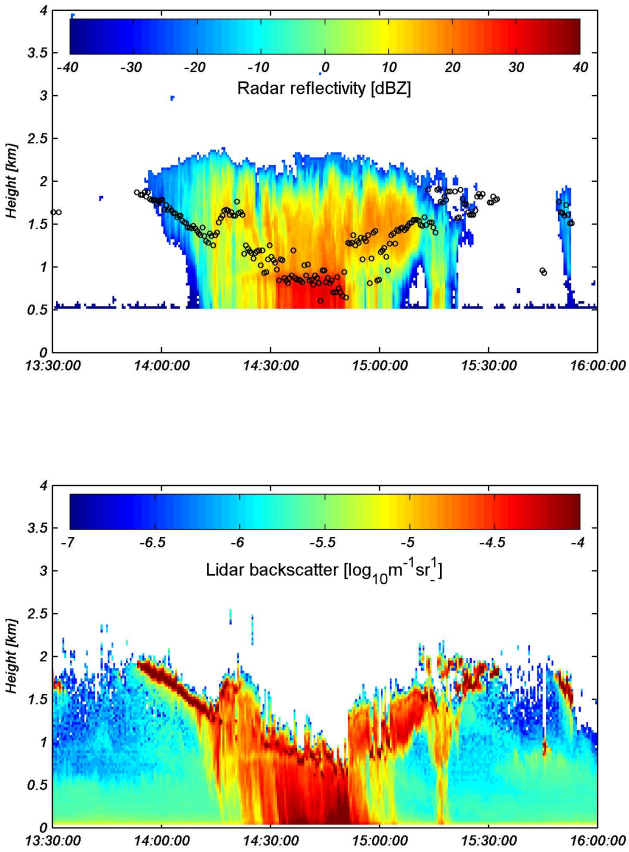

Fig. 2. Time series of vertically pointing cloud radar (top panel) and lidar ceilometer (bottom panel) during flight B425. Black markers on the radar time series show the height range of the first cloud base detected by the lidar.

ACPD
11, 30797–30851, 2011

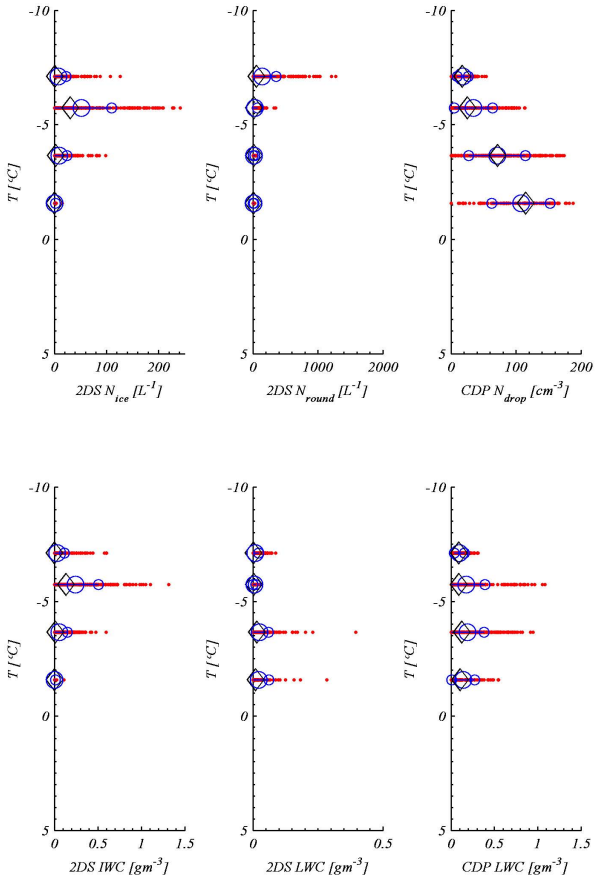

Fig. 3. In situ cloud particle number concentrations and ice and liquid water contents from flight B425, runs R1 to R7, as a function of ambient temperature. Red dots indicate a single 1 Hz data point; the black diamond is the median for the run and the large blue circle is the mean. The two smaller interconnected blue circles are one standard deviation from the mean.

ACPD
11, 30797–30851, 2011

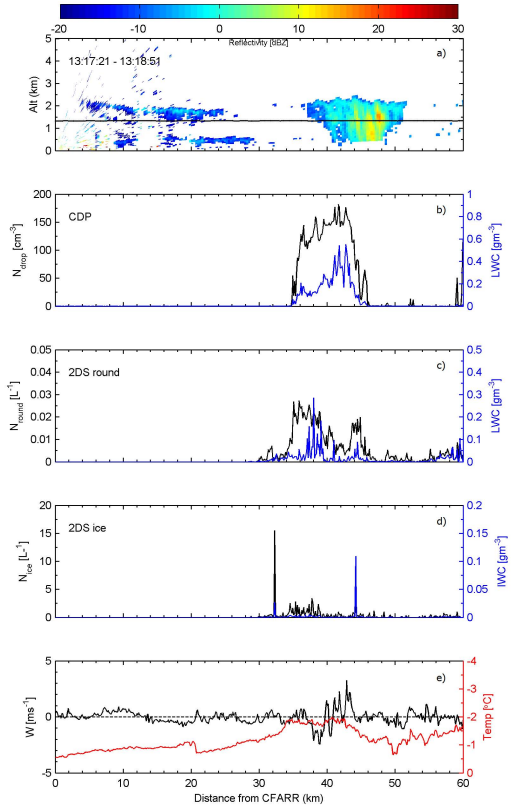

Fig. 4. Reflectivity from the 3 GHz CAMRa RHI scan along the 253° radial and GPS altitude (**a**, time of scan indicated in top left). In situ total particle number concentration (black lines, left axes) and mass loadings (blue lines, right axes) measured by: the CDP **(b)** as a function of distance from CFARR; 2DS round classification **(c)**, and 2DS ice classification **(d)**. Also shown **(e)**; in-situ temperature from the de-iced Rosemount sensor; vertical wind velocity from the 5-hole pressure port turbulence probe, all from run R1, inbound to CFARR.

ACPD
11, 30797–30851, 2011

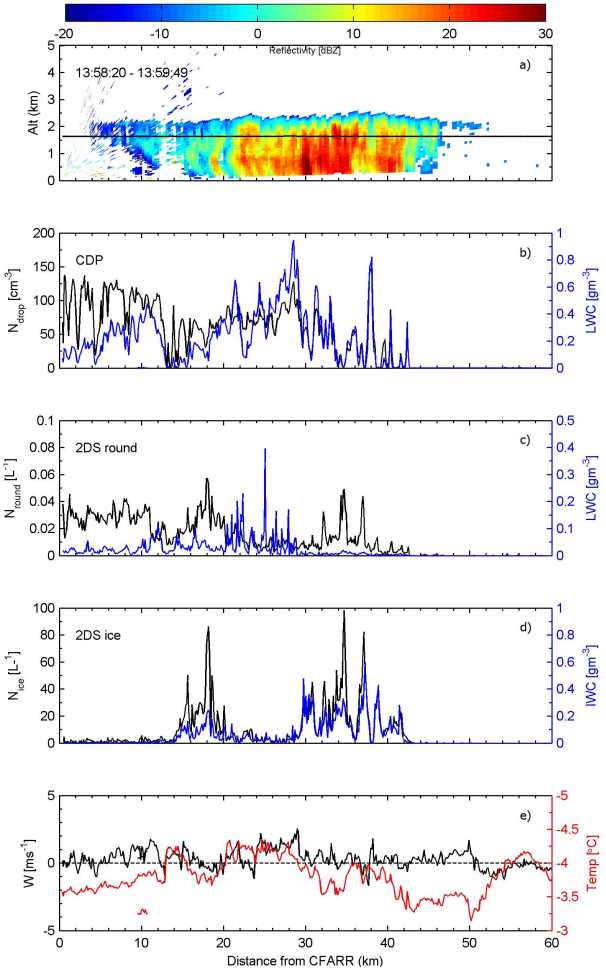

Fig. 5. Same as Fig. 4 but for Run R3, inbound to CFARR.

ACPD
11, 30797–30851, 2011

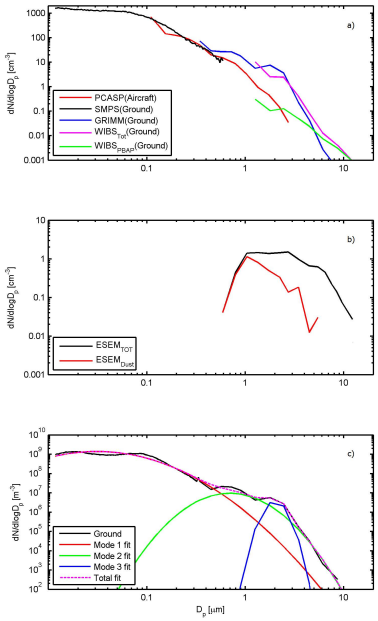

Fig. 6. Ground based and aircraft (run 2, below cloud) aerosol size distribution measurements. Comparison of aircraft and ground based aerosol size distributions **(a)**, including measured by WIBS (total particles and PBAP); Ground based SEM derived total aerosol and mineral dust size distributions **(b)**; The composite ground based aerosol size distribution with lognormal modes fitted to it for use in ACPIM investigations **(c)**. Here the black solid line is a composite of the ground based data; red, green and blue are different lognormal modes (1, 2, 3), fitted so that their superposition best fits the data (magenta line). The log-normal modal diameter, D_M (µm), dispersion (σ) and total number concentration (mg^{-1} of air) for each mode are: 0.0312, 0.9161, 3146; 0.6995, 0.5445, 12.94; and 2.01, 0.1795, 1.707 for modes 1, 2 and 3 respectively.

ACPD
11, 30797–30851, 2011

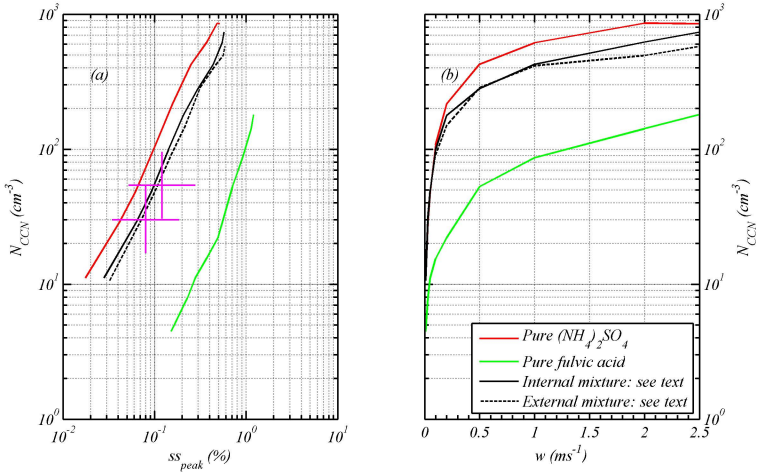

Fig. 7. (a) The results of parcel model simulations predicting the CCN concentration for different prescribed up-draught speeds plotted against the peak super-saturation attained, for different assumptions regarding mixed aerosol composition (see text). Also shown on the same plot are the measured CCN concentrations at super-saturations of 0.08 and 0.12 % in the air below cloud base (from aircraft run R2 at 750 m altitude). The best agreement is seen when the aerosol is assumed to be an external mixture (see text); **(b)** shows the modelled CCN concentrations plotted against updraft speed for the same cases.

ACPD
11, 30797–30851, 2011

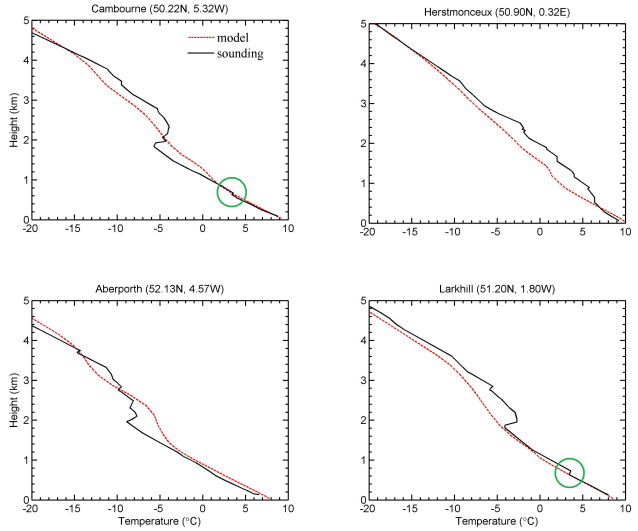

Fig. 8. Temperature profiles from radiosonde data (black) and the WRF model simulation (red) at selected locations. All profiles are taken at 12:00 UTC on the 22 January 2009. Note the small inversion just below cloud base at ~750 m in the Larkhill and Cambourne soundings (green circle).

ACPD
11, 30797–30851, 2011

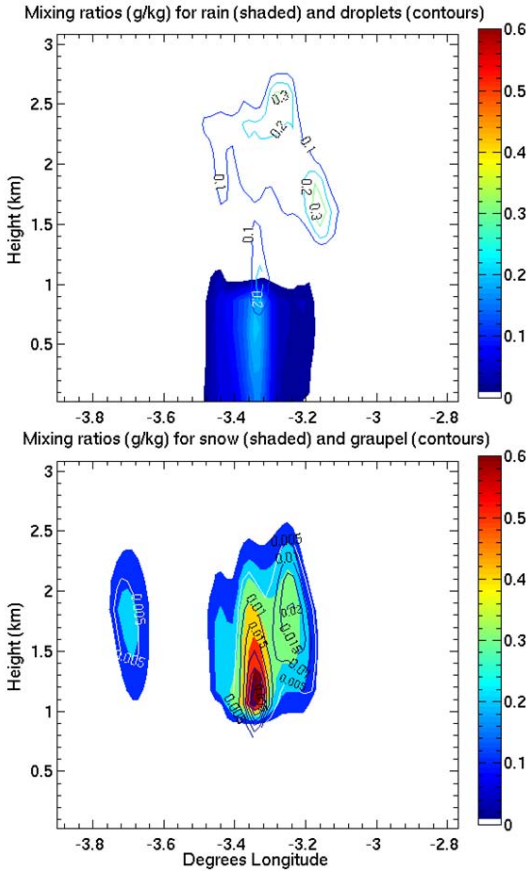

Fig. 9. Meridional cross-sections from model output at 51 degrees N at time 12:00 UTC. Top: liquid mixing ratios (rain and droplet categories); Bottom: ice mixing ratios (snow and graupel categories). Plots are in units of g kg^{-1}.

ACPD
11, 30797–30851, 2011

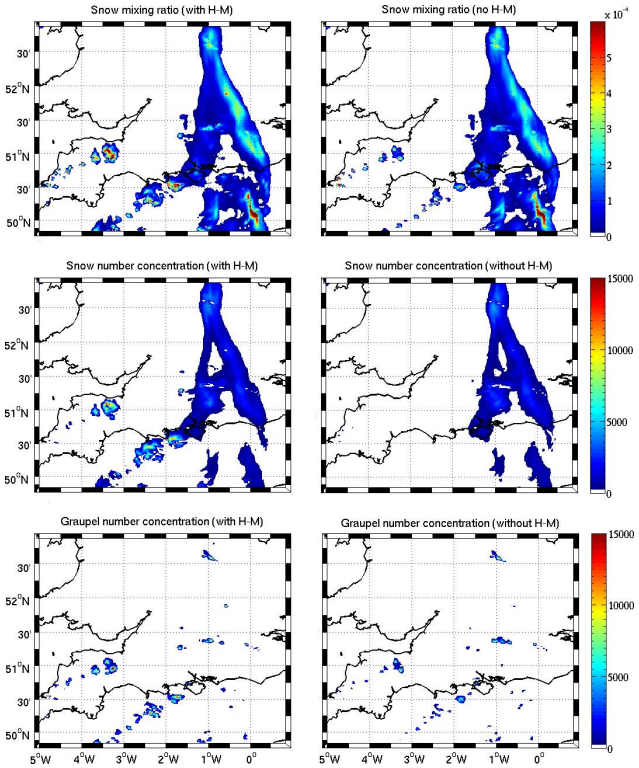

Fig. 10. WRF modelling results; Top panel: Snow mixing ratio (kg/kg) at 12:00 UTC and model level ll (1.42 km) for WRF simulation with HM (left) and without (right). The Chilbolton location is at 51.15 N, 1.45 W. Middle panel: same as top panel but for snow number concentration (kg^{-1}). Bottom: Same as middle panel but for graupel number concentration (kg^{-1}).

ACPD
11, 30797–30851, 2011

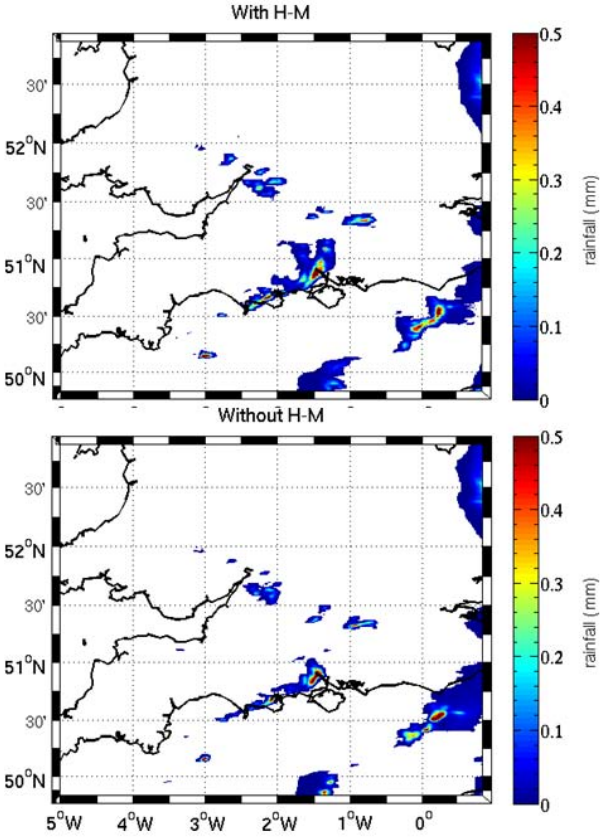

Fig. 11. Surface precipitation accumulated between 14:25 UTC and 14:30 UTC for: WRF with HM (top); WRF without HM (bottom).

ACPD
11, 30797–30851, 2011

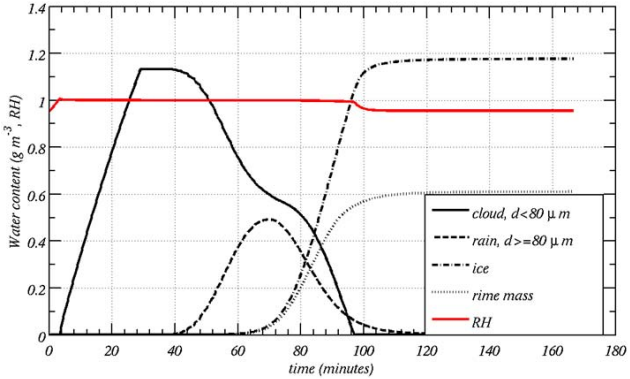

Fig. 12. Plot of modeled cloud, (d <80 µm), rain (d >80 µm), ice, and rimed water contents (g m^{-3}), as a function of time. with DeMott parameterisation shifted by 8 °C, and lower aerosol concentration reduced by a factor of 6 (see text).

ACPD
11, 30797–30851, 2011

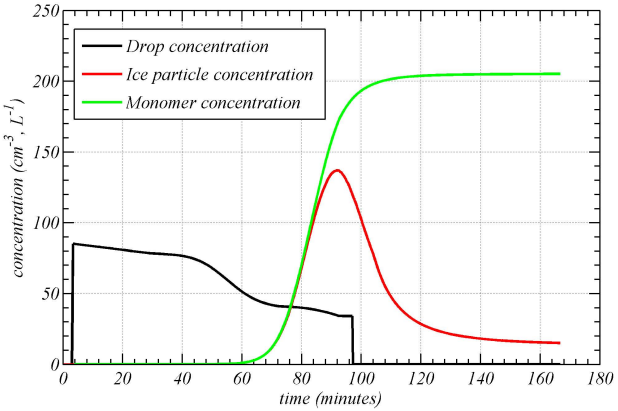

Fig. 13. Concentrations from the model with low aerosol and HM switched on where a monomer is defined as being a single ice crystal. Note that the prediction of ~90 cm^{-3} of drops is consistent with that measured at cloud base (Fig. 3). Ice particle concentrations far in excess of that predicted by the primary ice nucleation scheme, which predicts less than 1 L^{-1} at this temperature, are consistent with the observations. They peak at ~100 L^{-1}, but are more typically ~40 L^{-1}. The reason for this in the model is aggregation reduces the number of particles quite effectively.

ACPD
11, 30797–30851, 2011

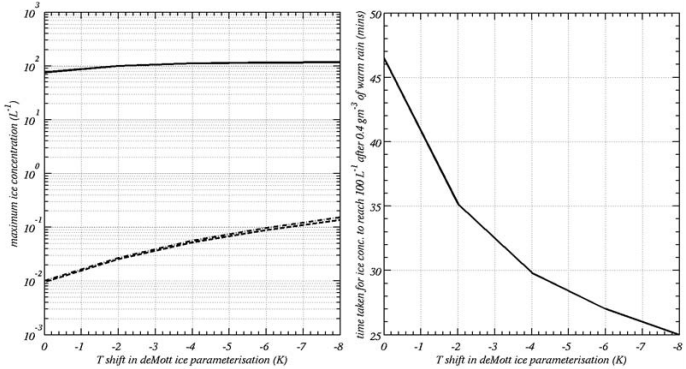

Fig. 14. Left: Plot showing the maximum in ice particle concentration in the model when the input temperature for the DeMott et al. (2010) ice nucleation parameterisation is shifted by the amount specified on the x-axis. Solid line, HM on with "low" aerosol input; dashed line, HM on with "high" input; dot-dashed line, HM off with "low" aerosol input. Right: time taken for the ice concentration to reach 100 L^{-1} following the onset of warm rain within the model as a function of temperature shift. At the higher temperature shifts the time is 25 min, while at the lower shifts it is almost twice as long.

ACPD
11, 30797–30851, 2011